

RESEARCH ARTICLE

The dry-season low-level cloud cover over western equatorial Africa: A case study with a mesoscale atmospheric model

Alexandre Berger¹  | Pierre Camberlin¹ | Julien Pergaud¹ |
Yseut Bahuet-Bourret² | Raffael Aellig³ | Olivier Champagne^{4,5}

¹Centre de Recherches de
Climatologie/Biogéosciences, Université
Bourgogne Europe, Dijon, France

²Universitat de les Illes Balears, Palma,
Spain

³Institute of Meteorology and Climate
Research, Karlsruhe Institute of
Technology, Karlsruhe, Germany

⁴Institut des Géosciences de
l'Environnement (IGE), Université
Grenoble Alpes, Grenoble, France

⁵Institute of Engineering and
Management, Université Grenoble Alpes,
Grenoble, France

Correspondence

Alexandre Berger, Centre de Recherches
de Climatologie/Biogéosciences,
Université Bourgogne Europe, Dijon,
France.

Email: alexandre.berger@u-bourgogne.fr

Funding information

Agence Nationale de la Recherche,
Grant/Award Number:
ANR-19-CE01-0021; Deutsche
Forschungsgemeinschaft, Grant/Award
Number: DFG FI 786/5-1

Abstract

A persistent low-level cloud cover (LCC) is a major climatic feature of western equatorial Africa during the long dry season (June–September). We investigate the ability of the mesoscale atmospheric model Meso-NH at 2-km horizontal grid spacing, forced by ERA5 reanalysis data, to simulate the LCC features. We chose a six-day period in June 2008, presenting temporal changes in cloud cover, to better understand the atmospheric mechanism associated with the LCC formation. The main meteorological variables of the model are firstly validated extensively against tri-hourly station data and ERA5. The LCC diurnal cycle shows an early-morning maximum consistent with station data, then a decrease in the afternoon which matches the evolution of the stratiform cloud cover, but some of the transition to cumulus clouds is missed. Discrepancies are found with respect to satellite data, but the latter have issues of reliability. Over the ocean, Meso-NH overestimates the LCC compared to satellite data, while ERA5 underestimates it. Over land, Meso-NH enabled the depiction of subregionally coherent LCC dynamics in relatively good agreement with observations, though discrepancies often occurred on individual days. This result does not depend on methodological issues such as the cloud overlap assumption or the low-level cloud fraction threshold retained to define cloudy observations. Dynamical analysis suggested that local and regional-scale wind direction changes, related to the synoptic weather pattern, are key to the maintenance or clear-up of the LCC in the afternoon. The LCC persistence is associated with surface westerlies advecting cooler maritime air increasing the lower-tropospheric stability. Moreover, the moistening of the top of the Planetary Boundary Layer promotes the formation of the LCC. These local atmospheric changes are driven by a mid-tropospheric easterly wave further north, a weakening of the Kalahari High over southern Africa and the weakening of the transequatorial flow.

KEYWORDS

low cloud, regional and mesoscale modeling, tools and methods, western equatorial Africa

1 | INTRODUCTION

The main dry season occurring from June to September in western equatorial Africa (WEA) shows a persistent low-level cloud cover (LCC) (Dommo et al., 2018), with typical seasonal mean cloud fractions as high as 50% to 80% (Champagne et al., 2023). Such a persistent LCC during the dry season is unusual for the tropics. It has major implications for the rainforest bioclimate in terms of solar radiation, temperature and evapotranspiration (Philippon et al., 2019; Philippon et al., 2022). This LCC has a non-convective origin (stratocumulus) and is related to the boundary layer cooling associated with low sea surface temperatures in the southern Atlantic Ocean (Dommo et al., 2018, 2022). However, its higher prevalence over the continent across a 200–400-km-wide band, covering the whole of Gabon and western Congo-Brazzaville, is still not fully explained.

WEA low-level clouds develop in late May to early June and last until September, or even October along the coast in the southern part of the region (Moron et al., 2023). Their prevalence is highest in the morning; they persist the whole day over the coastal plains and windward slopes of the mountain ranges, while inland on their leeward sides and over the plateaus, a clearing is observed in the afternoon, together with a change from stratocumulus to cumulus (Champagne et al., 2023). The cloud deck quickly develops again in the evening, as a result of moisture convergence and cooling below 600 m, while radiative cooling at the cloud top helps to maintain the cloud deck once it has formed (Dommo et al., 2022). Spatially coherent interannual variations are found in the occurrence of the LCC (Moron et al., 2023). Cloudy days are favored by lower sea surface temperatures over the eastern equatorial Atlantic Ocean, which enhance lower-tropospheric static stability and strengthen the lower arm of the zonal circulation between the Atlantic Ocean and the Congo Basin. Moron et al. (2023) also found that the El Niño/Southern Oscillation (ENSO) was a secondary driver, with warm events related to more frequent cloudy days, as a result of the mid-troposphere being warmer and exhibiting stronger easterlies.

Low-level clouds are often poorly simulated by climate models (Klein et al., 2017; Myers & Norris, 2016). The extensive stratocumulus cloud decks found over the southeastern Atlantic Ocean are underestimated by both atmospheric and coupled global climate models (Hu et al., 2008; Nam et al., 2012; Richter & Tokinaga, 2020; Xu et al., 2014). Over the continent, most coupled simulations from Phase 6 of the Coupled Model Intercomparison Project (CMIP6) also strongly underestimate the very dense stratiform cloud fractions (about 60%–80%) found over WEA in June–September (Camberlin et al., 2023).

In southern West Africa (SWA), global climate models show a widespread cloud cover in their simulation of the mostly nocturnal low-level clouds which develop during the July–September season (Hannak et al., 2017). Many models display an underestimation of cloud cover, an overestimation of cloud mean height, and a too weak diurnal cycle. Over the same region, Adler et al. (2017) carried out high-resolution numerical simulations (2.8 and 0.5 km) on the COSMO (CONsortium for Small-scale MOdeling) non-hydrostatic regional weather model. They pointed to several processes associated with SWA low-level clouds variability, namely a nocturnal cooling caused by horizontal advection in the southwesterly flow, vertical cold air advection due to gravity waves, and upward motion upstream of existing clouds. Kniffka et al. (2019) additionally demonstrated that relatively minor simulation errors of low-level cloudiness can have substantial impacts on large-scale SWA precipitation. Even though some of the large-scale circulation features affecting low-level cloudiness in SWA and WEA are similar, there are some differences between the two regions, like the presence of extensive rainforests over WEA.

In this paper, we assess the capability of the mesoscale non-hydrostatic atmospheric model Meso-NH (Lac et al., 2018) to reproduce the LCC over WEA and its characteristics (geographical extent, diurnal cycle, day-to-day variations). A few studies have examined the capability of regional models to represent WEA climates (Fotso-Kamga et al., 2020; Fotso-Nguemo et al., 2017; Vondou & Haensler, 2017), sometimes based on Coordinated Regional Downscaling Experiment (CORDEX) simulations (Haensler et al., 2013; Taguela et al., 2020) but they were generally confined to examining precipitation, temperature and wind patterns, with no information on dry-season cloudiness. As an exception, Komkoua Mbienda et al. (2022) succinctly analyzed seasonal total cloud cover over Central Africa using RegCM4.6. They found significant differences between the two Planetary Boundary Layer (PBL) parameterizations they used. However, their study did not separate convective clouds from low-level stratiform clouds, whose physical processes are completely different. More studies are available for the southeast Atlantic (Painemal et al., 2015; Seethala et al., 2018) but their results obtained over oceanic areas cannot be easily transposed to WEA.

An additional objective of the present study is to examine the local atmospheric mechanisms (changes in temperature inversion, moisture advection, etc.) and their large-scale drivers (zonal and meridional atmospheric circulation between the Atlantic Ocean and the Congo Basin) that are responsible for the day-to-day variations in the LCC extent over WEA. This issue has never been examined before by using a combination of observations,

satellites and mesoscale modeling. Further south, along the Atlantic coast in Namibia, Andersen et al. (2020) found that coastal low-level clouds exhibit day-to-day variations associated with sea-level pressure and Z500 patterns which control onshore advection of marine boundary layer air masses and cloud-top radiative cooling. However the climatological context is different from that of WEA, with a much stronger upwelling along the coast of Namibia, dry air advection from the continent, and southerly surges of relatively cold air, while WEA's equatorial location makes any control of the low-level clouds by mid-latitude systems less likely. Fuchs et al. (2017, 2018) analyzed the sensitivity of observed low-cloud fraction over a few subregions of the southeast Atlantic Ocean to their meteorological and aerosol environment. Marked regional differences were found, where lower-tropospheric stability, surface winds, free tropospheric temperature and long-distance air mass origins play uneven roles. Adebisi and Zuidema (2018) carried out a similar analysis but for the whole southeast Atlantic Ocean. None of these studies considered land areas in general and WEA in particular.

This study uses the Meso-NH model forced by ERA5 reanalysis data over a six-day period at the beginning of June 2008 which covers the early part of the 2008 dry season over WEA. In Section 2, we present the model setup and the databases used to document low-level cloud and other meteorological variables over WEA. Section 3 shows the results, by first examining the capability of Meso-NH to depict key meteorological fields at synoptic stations (Section 3.1) and in subdomains (Section 3.2) before analyzing LCC patterns and temporal variability (Section 3.3). The factors accounting for day-to-day low-level cloud variations are discussed in Section 3.4. Section 4 provides a summary of the main results.

2 | MODEL DESCRIPTION AND DATA

2.1 | Mesoscale atmospheric model Meso-NH

The simulation is performed with the mesoscale non-hydrostatic atmospheric model Meso-NH (<http://mesonh.aero.obs-mip.fr/mesonh>) version 5.4.4, developed jointly by the Laboratoire d'Aérodynamique and the Centre National de la Recherche Météorologique at Toulouse, France (Lac et al., 2018). Cloud microphysical processes are represented by the one-moment ICE3 scheme (Pinty & Jabouille, 1998) that includes six different types of hydrometeors. Surface processes and interactions with the atmosphere are simulated by the SURFEX model (Masson et al., 2013) coupled with Meso-NH. A 1.5-order

closure scheme for turbulence (Cuxart et al., 2000), an eddy-diffusivity mass-flux scheme for shallow convection (Pergaud et al., 2009), the KAFR scheme for the deep convection, the Rapid Radiative Transfer Model (Mlawer et al., 1997) for longwave radiation and the two-stream scheme (Fouquart & Bonnel, 1980) for shortwave radiation are used. Thermodynamic and other scalar variables are advected with the piecewise parabolic method (PPM) while the momentum variables are advected with a fourth-order centered scheme coupled to an explicit fourth-order centered Runge–Kutta time splitting (Lunet et al., 2017).

A study over Europe comparing Meso-NH with the WRF/CHEM mesoscale model showed a good agreement of simulated meteorological fields with surface hourly observations (Berger et al., 2016), although winds presented the largest bias for both models. Over the Sahara, another study intercomparing Meso-NH fields with those of the ALADIN and AROME area-limited models also showed a good performance of Meso-NH to reproduce ground-based and airborne observations (Chaboureau et al., 2016). The Meso-NH model provided a much more realistic vertical distribution of dust extinction. LCC has already been studied using Meso-NH, but it was based upon large-eddy simulation, that is to say eddies are explicitly resolved. Horizontal and spatial resolutions are so much lower (Brient et al., 2019; Delbeke et al., 2023). Delbeke et al. (2023) showed that Meso-NH is able to simulate low-level stratiform clouds in SWA during the wet monsoon season.

In this study, the computational domain extends over WEA and the surrounding regions, including part of the Gulf of Guinea (Figure 1). It includes two nested domains. The parent (coarser grid) domain (1) is composed of 400×400 grid points with a horizontal resolution of 6 km, from 1° W to 21° E and from 12.5° S to 10° N. The finer domain (2) is located at the center of the parent domain ($6\text{--}14^\circ$ E, 5° S– 3° N, covering the whole of Gabon and the southwesternmost part of the Republic of Congo) and is composed of 480×480 grid points with a horizontal resolution of 2 km to resolve convection explicitly. One-way nesting is used between both domains so the following results are based on the finer domain. The vertical grid has 52 levels for the two nested domains, stretched to allow a better representation of the boundary layer, which is essential to get closer to the real dynamic circulation. The lowest level is at 10 m and the highest one is at about 15 km. The timestep in the innermost domain is 15 s and the simulation is driven by ERA5 reanalysis as initial conditions and every 6 h as boundary conditions.

For the analysis of the simulation, three subdomains roughly parallel to the southwestern coast of Gabon are defined (Figure 1, right panel), namely “offshore” (subdomain1, over the Gulf of Guinea south of the Equator),

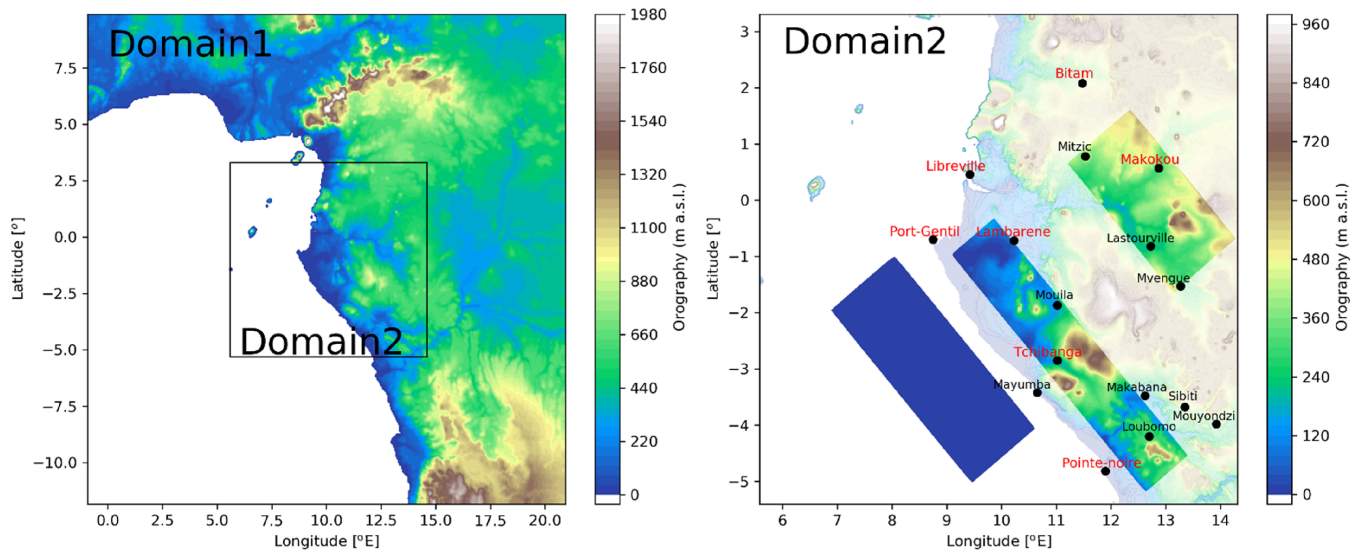


FIGURE 1 Horizontal representation of the two nested simulated domains and their orography. The network of SYNOP stations as well as the three subdomains are also indicated on the right panel. In red, the seven stations used to depict low-level cloud cover variations. [Colour figure can be viewed at [wileyonlinelibrary.com](https://onlinelibrary.wiley.com/doi/10.1002/qj.4962)]

“coastal” (subdomain2, including coastal plains and first hills) and “inland” (subdomain3, comprising much of the upper Ogooué valley and adjoining plateau escarpments). Champagne et al. (2023) showed that the low-level cloud occurrence and its diurnal cycle partly differ between these three subdomains, with a more persistent cloud cover over the coastal plains and west-facing hillsides.

2.2 | ERA5 reanalysis

ERA5 is the fifth generation of climate reanalysis data from ECMWF (European Centre for Medium Range Weather Forecasts). ERA5 replaced ERA-Interim, which ceased to be produced at the end of August 2019 (C3S, 2017), and includes considerable improvements and higher horizontal, temporal and vertical resolutions (Hersbach et al., 2020). The data are at a native horizontal resolution of 31 km, made available on a 0.25-degree grid, and resolve the atmosphere at 137 levels from the surface to a height of 80 km, on an hourly time-scale. ERA5 is processed with the Integrated Forecasting System (IFS).

The low-level cloud fraction (LCF) is a single level field in ERA5 which is calculated from cloud occurring on model levels with a pressure greater than 0.8 times the surface pressure (see Section 2.5 for more explanations). The LCF is also available per vertical level and this variable is only used in this study on Figure 10.

ERA5 has been extensively used to depict Central Africa climate dynamics (e.g., Kenfack et al., 2023; Kuete et al., 2023; Ouhechou et al., 2023). Its representation of WEA low clouds was found to be fairly consistent with synoptic observations (Champagne et al., 2023;

Dommo et al., 2022), provided that convective clouds which sometimes develop in the afternoon are screened out (Moron et al., 2023).

2.3 | Observations

In addition to the large-scale reanalysis data from ERA5, Meso-NH simulations were validated against two types of observations described below: ground-based (synoptic) and satellite data.

2.3.1 | Ground-based observations

Simulated surface meteorological fields were compared to three-hourly observed synoptic data archived in the Integrated Surface Database (ISD) managed by the United States National Centers for Environment Information (NCEI), which provides public access to SYNOP reports of meteorological surface parameters over WEA. Wind direction, wind speed, temperature, cloud information and relative humidity were used for this study. Sixteen synoptic stations are included in the inner domain (Figure 1, right panel), but only seven of them (in red) have been reporting weather observations over the period of study, with very few night-time records.

Ground-based information on low-level clouds at the same stations was extracted from a comprehensive database of cloud cover assembled for WEA (Aellig et al., 2022) based on different meteorological datasets and mostly based on SYNOP reports as well. LCF as reported from trained observers is provided in octas (from zero for

clear sky to eight for fully covered sky) for clouds whose base height is below 2000 m. The cloud type (stratiform or cumuliform) is also reported. The presence of low-level clouds is asserted whenever the LCF is greater than or equal to four octas (over half of the sky covered by clouds). We distinguish between stratiform (mostly stratocumulus, typical of the dry season) and cumuliform low clouds when computing cloud statistics. Data on the height of the cloud base were also separately extracted from the raw SYNOP messages.

2.3.2 | Satellite products

Two satellite LCC datasets, both derived from the Spinning Enhanced Visible and infrared Imager (SEVIRI), are used in this study: the Satellite Application Facility on Support to Nowcasting and Very Short Range Forecasting cloud types (SAFNWC-CT) and the night microphysical scheme (NMS).

Based on brightness temperature and reflectance from the SEVIRI sensor on-board the Meteosat Second Generation geostationary satellite (Derrien & Gléau, 2005), SAFNWC-CT is a classification into 14 cloud types at 3-km spatial and 15-min temporal resolutions. We consider that a LCC is present in a grid cell when either “very low clouds” (up to 2000 m a.s.l.) or “low clouds” (2000–3500 m a.s.l. to take into account the relief) are detected. When higher clouds are detected, the corresponding LCC observation is viewed as missing since no assumption can be made on the presence or absence of low-level clouds below the higher clouds. Although the SAFNWC-CT data cover both night- and daytime, the absence of reflectance data makes it difficult to detect low-level clouds at night (Champagne et al., 2023). Hence, SAFNWC-CT data were used to cover only the time-slots from 0700 to 1700 UTC.

The NMS (Lensky & Rosenfeld, 2008) is based on a combination of three infrared channels of SEVIRI, with thresholds capable of detecting cloud tops below 3000 m. More information on how the low clouds are screened is provided in Champagne et al. (2023). Low-level cloud occurrence is extracted at a 3-km resolution.

Both products are available at 15-min timesteps and have been averaged to hourly data.

2.4 | Simulation period

The simulation was performed over a seven-day period starting from 4 June 2008 0000 UTC to 11 June 2008 0000 UTC. The spin-up period to develop proper mesoscale and large-scale circulations was 4 June (a 24-h spin-up is usually adopted in such regional simulations; Bonekamp

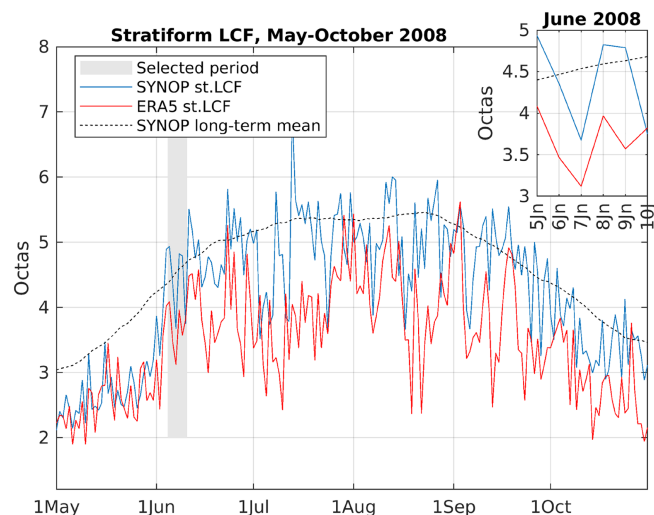


FIGURE 2 Areal-mean daily stratiform low-level cloud fraction (LCF) (octas) from seven synoptic stations in Gabon and southern Congo (SYNOP, in red on Figure 1) and for the corresponding ERA5 grid points, May to October 2008. The inset shows the subperiod retained for the study. [Colour figure can be viewed at [wileyonlinelibrary.com](https://onlinelibrary.wiley.com/doi/10.1002/qj.4962)]

et al., 2018) and therefore is not used in the following analyses. This seven-day period is at the beginning of the dry season, when the low-level cloud deck has already developed over WEA (Figure 2). It was retained because this is a period showing a relatively large daily variability of LCF, as evidenced from both ERA5 outputs and surface SYNOP observations (Figure 2). Although ERA5 underestimates the dry-season low-level cloud cover by about one octa compared to observations, temporal variations agree reasonably well, with a correlation of 0.73 ($n = 184$) between the two datasets during the whole season, and 0.33 after deseasonalization (removal of low-pass filtered long-term daily mean), both significant at $p < 0.001$. Over the period of simulation, both datasets show higher LCF values on 5, 6, 8 and 9 June, while more clear skies developed on 7 and 10 June.

The average meteorological conditions from ERA5 for the six-day period (5 to 10 June) are shown on Figure 3. The near-surface atmospheric circulation, representative of the austral winter season, is characterized by two high-pressure systems (Figure 3a). An anticyclone over the southern Atlantic Ocean (St-Helena anticyclone) drives strong southeasterly winds, which feed into the West African monsoon further north (Dezfuli, 2017) and another anticyclone over central southern Africa drives mid-tropospheric easterlies, known as the southern African Easterly Jet (Adebiyi & Zuidema, 2016; Nicholson & Grist, 2003).

Over our region of interest, the wind blows from the south along the coast (Figure 3b). ERA5, in reasonable

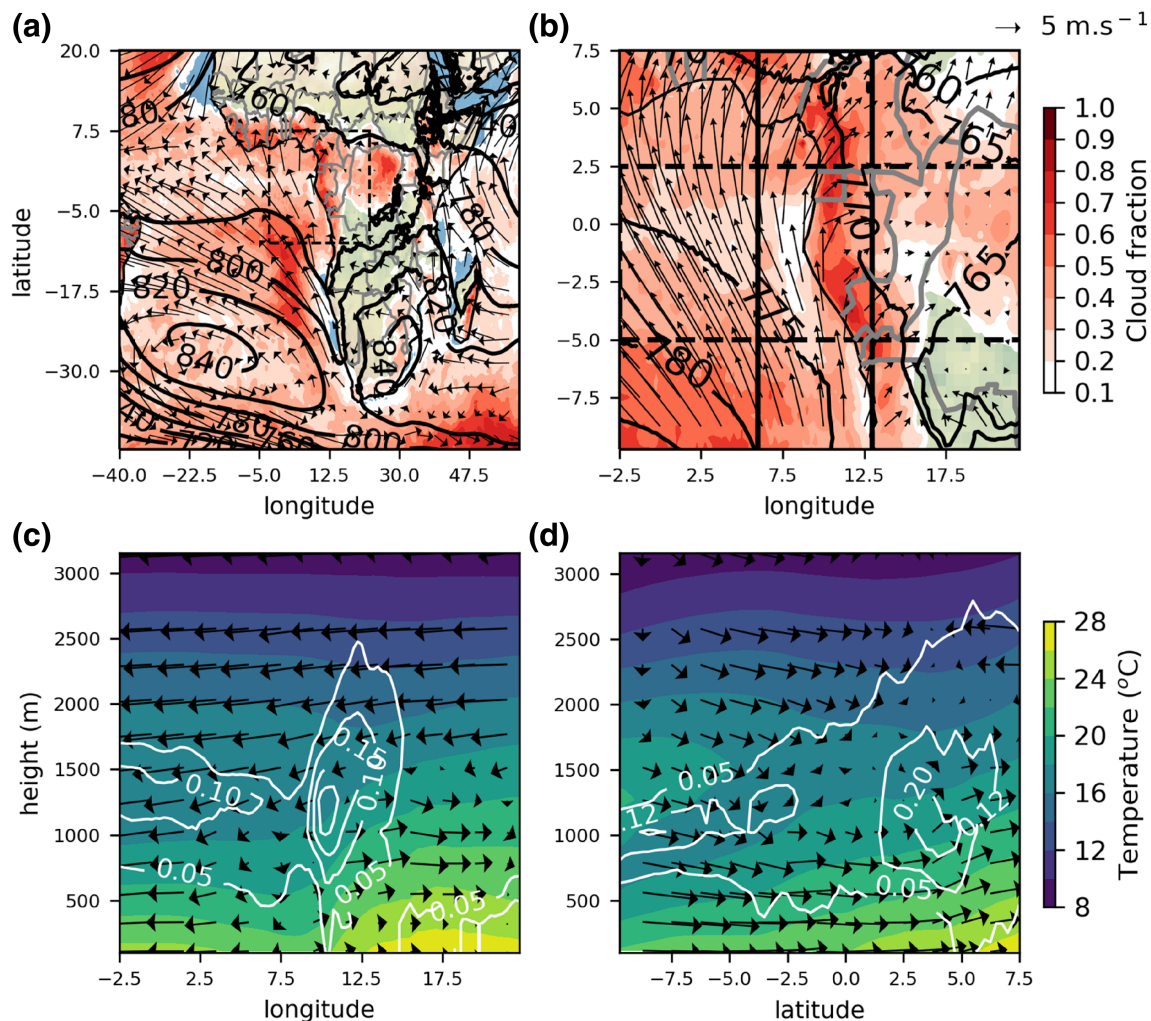


FIGURE 3 ERA5 mean meteorological synoptic patterns averaged over the six-day period 5–10 June 2008 at 925 hPa (a,b), along a longitudinal cross-section (dashed rectangle) averaged from 5° S to 2.5° N (c) and a latitudinal cross-section (continuous rectangle) averaged from 6° E to 13° E (d). For panels (a) and (b), 925 hPa winds are shown as black vectors, geopotential height as black isocontours (in dam) and low-level cloud fraction in red-colored shadings (blue and green shadings when CF < 0.1 over sea and land, respectively). For cross-sections, horizontal wind combined to vertical velocity are shown as black vectors, temperature as colored shadings, and cloud fraction by white isocontours. [Colour figure can be viewed at [wileyonlinelibrary.com](https://onlinelibrary.wiley.com/terms-and-conditions)]

agreement with observations (Dommo et al., 2018), displays the largest LCF along a 300-km wide coastal belt, a feature characteristic of the mean conditions during the JJAS dry season. These low-level clouds are most apparent around 1000-m height between 8.75° E and 12° E and between 8° S and 2.5° S (Figure 3c,d). A temperature inversion is clearly visible in the southern hemisphere, with warmer air at 1500-m height (20°C near 8° S) than below 1000-m height (17°C). This inversion is associated with subsiding southerlies and it vanishes near the equator (Figure 3d). The LCC separates two air flows, implying a shear. At the surface, south-westerlies prevail east of the coastline, while above 1000 m they are replaced by easterlies to southeasterlies (Figure 3c,d).

2.5 | Methodology for LCC computation

The LCC data (i.e., SYNOP observations, NMS and SAFNWC satellite products and reanalyzed ERA5 fields) are compared to Meso-NH cloud information. These products do not have the same horizontal resolution. Thus, the fields of each product are regridded on the Meso-NH grid by finding the nearest grid point of the simulation. However, the description of the LCC is quite different across all these products. It is therefore necessary to define a methodology enabling an appropriate comparison of the Meso-NH simulation with the other datasets. When we do the comparison between modeled and satellite LCC over subdomains, we only look at grid points in NMS and SAFNWC where high clouds are not present.

Indeed, it avoids the biases linked to the masking of LCC by high clouds for satellite data.

While the other LCC data are two-dimensional (2D) fields, Meso-NH provides the cloud fraction (from 0 to 1) as 3D data for each vertical model level and for each grid point. Thus, it is necessary to translate the 3D cloud fraction information simulated by Meso-NH, into a 2D integrated vertical information representing the cloud cover. Two cloud overlap assumption methods allow us to compute the total cloud cover resulting from the knowledge of the cloud fraction of multiple cloud layers (Morcrette & Fouquart, 1986). The first one is the maximum-random-overlap assumption (Räisänen, 1998), whereby vertically continuous clouds are assumed to be maximally overlapped, and was applied in the ECMWF longwave radiation scheme (Morcrette, 1989, 1991). The second one is the random-overlap assumption, whereby clouds at different heights that are separated by an entirely cloud-free model level are randomly overlapped (Geleyn & Hollingsworth, 1979). Hogan and Illingworth (2000) have used a generalized form of cloud overlap in which the total cloud fraction is described by a linear combination of maximum and random. In this method, the total cloud fraction is always between random and maximum overlap. LCC fields computed in ERA5 are based upon this last method (Barker, 2008), applied to the 3D cloud fraction obtained from the Tiedtke cloud scheme (Tiedtke, 1993) at each grid box.

The results of the two cloud overlap assumptions are discussed in Section 3.3. Other methodological choices in the characterization of the low-cloud cover are presented in the same section.

3 | SIMULATION RESULTS

Before a detailed examination of LCC patterns, an overall evaluation of Meso-NH key meteorological variables

is carried out through a comparison at synoptic stations (Section 3.1), then with ERA5 over the three above-defined subdomains and in the vertical (Section 3.2). Section 3.3 is then devoted to the ability of Meso-NH to reproduce the observed LCC and Section 3.4 to the mechanisms responsible for the LCC formation.

3.1 | Comparison of key surface meteorological variables at synoptic stations

Table 1 compares the SYNOP tri-hourly available synoptic observations over the seven stations to Meso-NH and ERA5 data (nearest grid points). Note that the number of tri-hourly available observations varies according to the variable. Table 1 provides the mean, the mean errors (three-hourly bias averaged over n_{obs}) and the root-mean-squared errors (RMSE). Each value has its associated standard deviation. The RMSE is obtained from the six-day average of square root of the mean squared differences between the models and the observations over all the nearest grid points corresponding to the stations. The standard deviations for RMSE translate the dispersion of the three-hourly RMSE over the six-day period.

Meso-NH and ERA5 have a negative 2-m temperature bias (T2) compared to observations (-1.77°C for Meso-NH, -1.30°C for ERA5). For 2-m relative humidity (RH2), Meso-NH shows a smaller bias than ERA5, and a slightly smaller RMSE, although still quite large. Wind speeds at 10 m (WS10) are lower than observations in both Meso-NH and ERA5, though the bias is greater in the former one. The average surface wind direction at 10 m (WD10; 0° from North– 90° from East) is southsouthwesterly (189 to 195°) as for the observations, with a slightly higher negative bias in Meso-NH than in ERA5. For all the variables examined, biases with respect to observations have the same sign in Meso-NH and ERA5. Some of these

TABLE 1 Comparison between three-hourly SYNOP observations at seven stations (Libreville, Makokou, Port-Gentil, Lambaréné, Pointe-Noire, Tchibanga and Bitam), and Meso-NH (MNH) and ERA5 at the nearest grid point over the six-day period, for selected surface variables.

	T2 ($^{\circ}\text{C}$)		RH2 (%)		WS10 ($\text{m}\cdot\text{s}^{-1}$)		WD10 (degrees from north)	
	MNH	ERA5	MNH	ERA5	MNH	ERA5	MNH	ERA5
n_{obs}	228		222		117		140	
Mean	23.46 ± 1.43	23.93 ± 1.25	86.09 ± 6.36	87.65 ± 5.37	2.10 ± 0.72	2.77 ± 0.91	188.97 ± 42.05	195.33 ± 29.98
Mean error	-1.77 ± 1.40	-1.30 ± 1.14	2.19 ± 5.37	3.75 ± 4.77	-0.78 ± 1.36	-0.11 ± 1.26	-12.57 ± 44.36	-6.21 ± 42.33
RMSE	2.96 ± 1.12	2.58 ± 0.99	9.43 ± 4.58	9.92 ± 5.58	1.92 ± 0.97	1.48 ± 0.70	47.13 ± 26.40	44.70 ± 29.45

Note: Standard deviation of each statistical parameter is added near each value.

Abbreviations: n_{obs} , number of three-hourly observations; RH2, relative humidity at 2 m; RMSE, root-mean-squared error; T2, temperature at 2 m; WD10, wind direction at 10 m; WS10, wind speed at 10 m.

biases are inherent to the station-to-grid-point comparison which induces some discrepancies in elevation (up to 100 m of difference in altitude for instance) and in land cover (e.g., for coastal stations which are very close to the sea). The RMSE and the standard deviations over the stations available are similar for ERA5 and Meso-NH for the four surface variables suggesting a close performance for simulating surface meteorology.

The mean diurnal variations of these four surface parameters at the available stations and co-located Meso-NH and ERA5 grid points are plotted on Figure 4. Caution should be exerted as the number of stations greatly reduces at night and represents only coastal meteorological conditions (Libreville, Port-Gentil and Pointe-Noire). That is why we have to analyze daytime (from 0600 to 1800 UTC) and night-time (2100 to 0300 UTC) separately.

At daytime, observed T2 increases from 0600 UTC to a peak at 1500 UTC before strongly decreasing. Meso-NH and ERA5 reproduce well this diurnal evolution. However, the afternoon values (1500 and 1800 UTC) are slightly

underestimated in ERA5 and Meso-NH (-1 to -2°C at 1800 UTC), but strongly depending on stations. At night, at the coastal stations, Meso-NH is up to -3°C cooler (at 2100 UTC) than the observations. ERA5 underestimates T2 too, but to a lesser extent. RH2 goes down from a peak at 95% in the early morning to a minimum of 70% at 1200 and 1500 UTC. Both Meso-NH and ERA5 show the same pattern although at daytime the extended lower part of the box plots suggests that at some stations the air is drier (up to -20%) than in the observations. WS10 observed during the daytime is low ($2\text{--}3\text{ m}\cdot\text{s}^{-1}$) and does not vary a lot. Both Meso-NH and ERA5 slightly underestimate it (less than $1\text{ m}\cdot\text{s}^{-1}$) with respect to SYNOP observations as seen in Table 1. At night, the observed WS10 is stronger, though this is biased by the fact that only coastal stations are then available. This is well replicated by Meso-NH and ERA5 only at 0300 UTC. For WD10, the observations at the stations show southeasterlies from 0000 to 0900 UTC, and southwesterlies from noon to 2100 UTC. This is reasonably well reproduced by Meso-NH and ERA5, with biases generally between 10° and 30° .

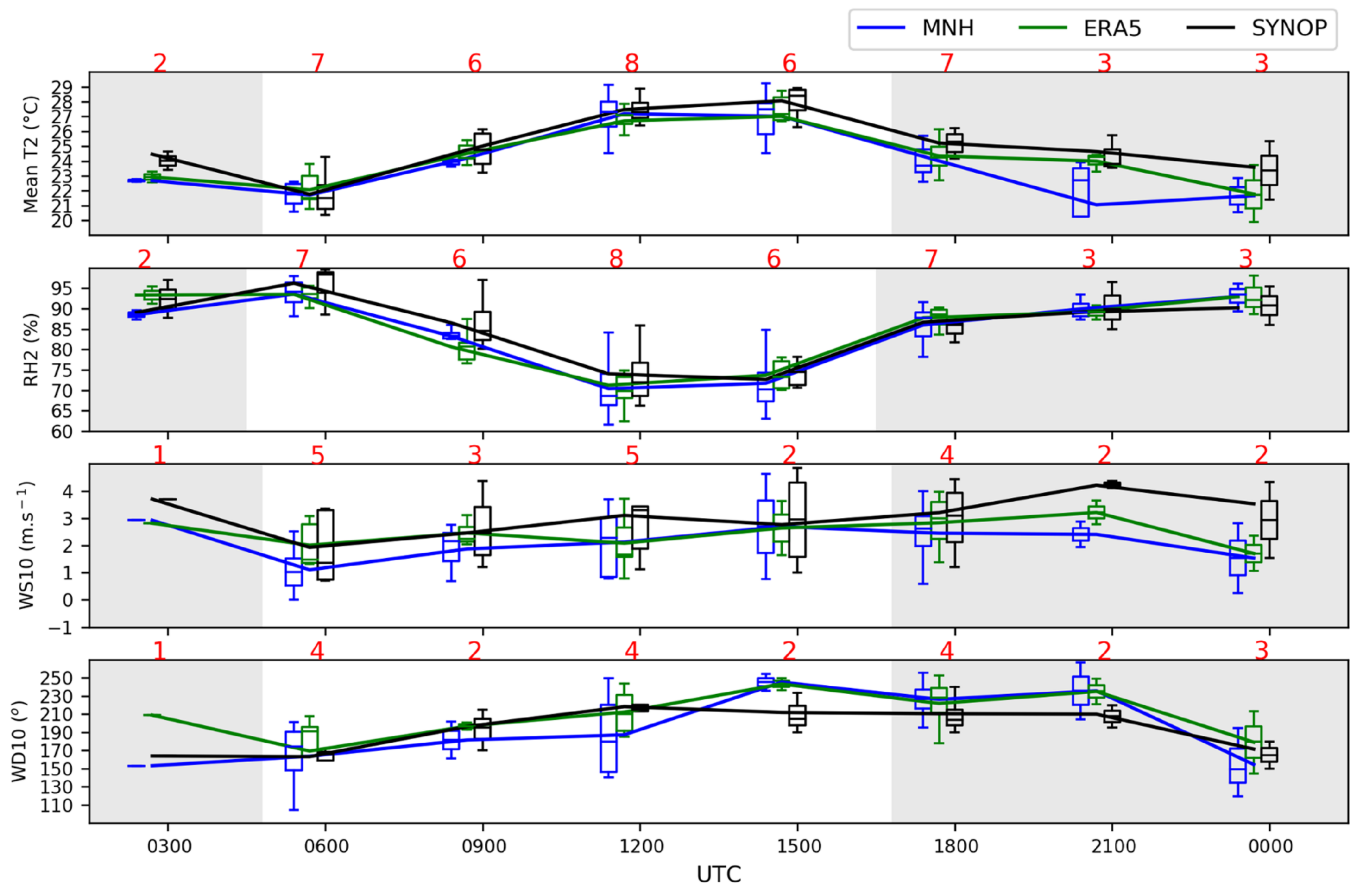


FIGURE 4 Mean diurnal variations of selected variables over the six-day period as a tri-hourly average of all available synoptic observations (black line), Meso-NH simulations (blue line) and ERA5 (green line) at the grid point nearest to the stations. The box plots show the distribution of the raw values for each product. Red number at top: number of available stations. The gray band denotes night-time. RH2, relative humidity at 2 m; T2, temperature at 2 m; WD10, wind direction at 10 m; WS10, wind speed at 10 m. [Colour figure can be viewed at [wileyonlinelibrary.com](https://onlinelibrary.wiley.com/doi/10.1002/qj.4962)]

3.2 | Comparison between ERA5 and Meso-NH over the subdomains and along cross-sections

For the three subdomains located on Figure 1, Table 2 provides the six-day means, spatially averaged Meso-NH outputs for near-surface parameters (T2, RH2, WS10, WD10), the planetary boundary layer height (PBLH) and the cloud mixing ratio (RC) integrated from the ground to 2000 m height to represent only low-level clouds. In Meso-NH and ERA5, the methods used for estimating the height of the boundary layer top are the parcel method (Seibert et al., 2000) and the bulk Richardson number method (Seidel et al., 2012), respectively. Additionally, Table 2 shows mean errors and RMSE with respect to ERA5. It must be stressed that they are to be interpreted as differences between the two datasets rather than actual errors. The RMSE is obtained from the six-day average square root of the mean squared differences between Meso-NH and ERA5 over all the grid points of a specific subdomain.

The 2-m temperature (T2) shows very small differences over the ocean (subdomain1), and only marginally larger over land (subdomains 2 and 3). The 2-m relative humidity (RH2) is the highest over the ocean (subdomain1) in both products with a moderate drying going inland (subdomains 2 and 3). Meso-NH tends to simulate slightly drier conditions than ERA5 over the ocean and somewhat wetter conditions inland. Mean biases in RH2 are small but the RMSE is much larger, indicating that temporal

and spatial variations are quite distinct between the two datasets. The mean wind direction at 10 m (WD10) from Meso-NH is close to that of ERA5. The winds have a south-westerly component over land and southeasterly direction off the coast. As for RH2, quite large RMSE values suggest more disagreement in the temporal variations of wind directions. Winds are stronger over the ocean (in both ERA5 and Meso-NH), and weaken as one goes inland. The weakening is much more evident in Meso-NH than in ERA5, as denoted by the negative mean errors. This could arise from the better-resolved local topography in Meso-NH which contributes to increased roughness and associated friction. The lower-tropospheric cloud mixing ratio (RC) also shows some discrepancies with ERA5. While the increased RC over land compared to the ocean is found in both Meso-NH and ERA5, with a maximum of low-level clouds over subdomain2 and a decrease further to the northwest in subdomain3, mean errors reverse between the two subdomains. RC is higher in Meso-NH than in ERA5 over the coastal plains, but lower than in ERA5 further inland. Importantly, RMSE values are large (always larger than the mean RC), suggesting a temporal mismatch in the cloud cover between Meso-NH and ERA5, which will be discussed below. Finally, the diurnal thermal exchanges (expressed by PBLH) between the ocean/soil and the lower troposphere are similar in Meso-NH and ERA5.

In order to better understand the discrepancies found between Meso-NH and ERA5, hourly variations of key surface meteorological variables are plotted over the six-day

TABLE 2 Meso-NH six-day averages in the three subdomains for T2, RH2, WS10, WD10, RC, and PBLH (see text). The mean error and RMSE are computed with respect to ERA5 data.

	T2 (°C)	RH2 (%)	WS10 (m·s ⁻¹)	WD10 (°)	RC (mg·kg ⁻¹)	PBLH (m)
Sub-domain1 “offshore”						
Mean	23.31	87.92	3.10	168.66	320	415.35
Mean error	−0.19	−1.73	−0.24	6.93	270	29.56
RMSE	0.44	4.15	1.22	46.61	70	123.12
Sub-domain2 “coastal”						
Mean	22.73	85.93	0.92	195.16	940	396.07
Mean error	−0.69	0.61	−0.54	−16.41	690	−0.98
RMSE	1.60	6.60	1.00	67.84	300	198.17
Sub-domain3 “inland”						
Mean	24.73	84.44	0.39	229.67	580	430.2
Mean error	0.38	2.12	−1.11	−0.74	440	−28.38
RMSE	1.20	6.99	1.09	67.88	390	198.67

Abbreviations: PBLH, planetary boundary layer height; RC, cloud mixing ratio; RH2, relative humidity at 2 m; RMSE, root-mean-squared error; T2, temperature at 2 m; WD10, wind direction at 10 m; WS10, wind speed at 10 m.

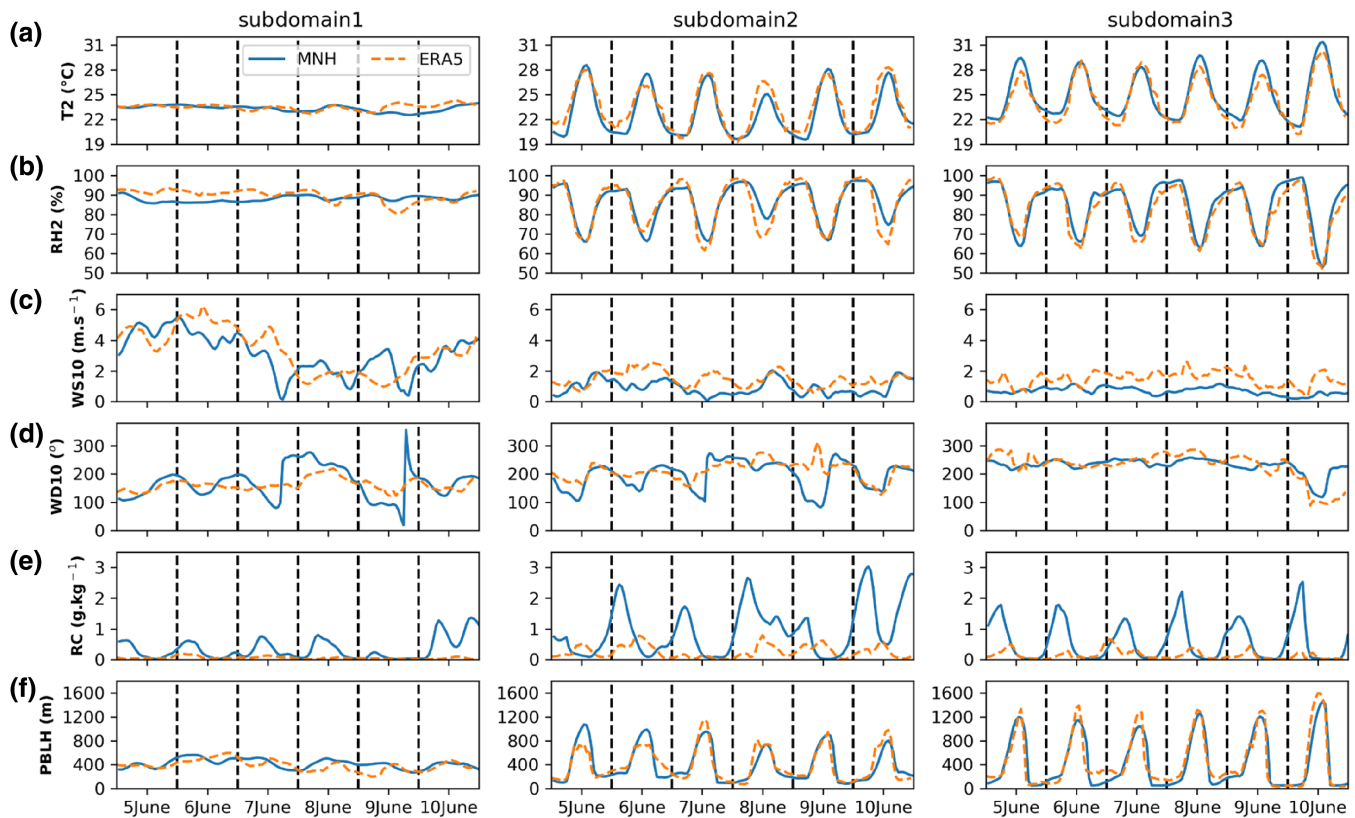


FIGURE 5 Hourly variation of meteorological fields for Meso-NH and ERA5 for the three subdomains for (a) temperature at 2 m (T_2); (b) relative humidity at 2 m (RH_2); (c) wind speed at 10 m (WS_{10}); (d) wind direction at 10 m (WD_{10}); (e) cloud mixing ratio (RC); and (f) planetary boundary layer height ($PBLH$). [Colour figure can be viewed at wileyonlinelibrary.com]

period for Meso-NH and ERA5 (Figure 5). The three subdomains are shown since major differences occur between the oceanic and the continental regions.

Over the ocean (subdomain1), there is very little variation over the six days for T_2 , RH_2 , and $PBLH$. This is particularly linked to the cold tongue that limits exchanges between ocean and atmosphere and restricts diurnal variations, including those of the LCC, in agreement with Painemal et al. (2015). WS_{10} and WD_{10} similarly do not show any clear diurnal cycle but they do vary from day to day. Although the general weakening of winds from 6 to 9 June in ERA5 is matched by Meso-NH, the two datasets show some differences in the temporal variations of both WS_{10} and WD_{10} , with larger fluctuations for Meso-NH.

Over the continent, the diurnal variations are much more pronounced. Both ERA5 and Meso-NH display the expected daytime warming, with RH_2 showing a concomitant decrease (65%–70% during daytime to more than 90% during night-time). The $PBLH$ diurnal cycle (low at night, then gradually rising to about 1200 m during the day) is also very similar between Meso-NH and ERA5, and follows that of T_2 . WS_{10} is very low, not exceeding 2 m.s^{-1} over the two subdomains. It remains weaker for Meso-NH than ERA5 all day long, especially over subdomain3. As in

subdomain1, wind directions show discrepancies between ERA5 and Meso-NH. Over subdomain2, a weak diurnal cycle is found in Meso-NH, which is absent in ERA5. Southeasterlies in the morning tend to switch to southwesterlies by the end of the afternoon and at night. In this subcoastal area, this suggests that Meso-NH better represents land–sea breezes than ERA5. On the morning of 9 June, a larger difference in wind direction occurs. While the wind blows from the southeast as every morning in Meso-NH, the wind in ERA5 blows from the west. Over subdomain3, the wind comes from the west except on 10 June where it suddenly blows from the east. The amount of low-level cloud formed is similar for Meso-NH and ERA5. However, a marked phase shift occurs with a maximum of low-level clouds several hours sooner for Meso-NH (late night) than for ERA5 (often around noon). These results explain the high RMSE values found in Table 2 for some variables (especially WD_{10} and RC) which denote partly distinct atmospheric variability between Meso-NH and ERA5, including for cloud dynamics which will be further examined in Section 3.3.

As a complement to the comparison between ERA5 and Meso-NH, west–east vertical cross-sections (Figure 6) depict the six-day mean low-level atmospheric patterns

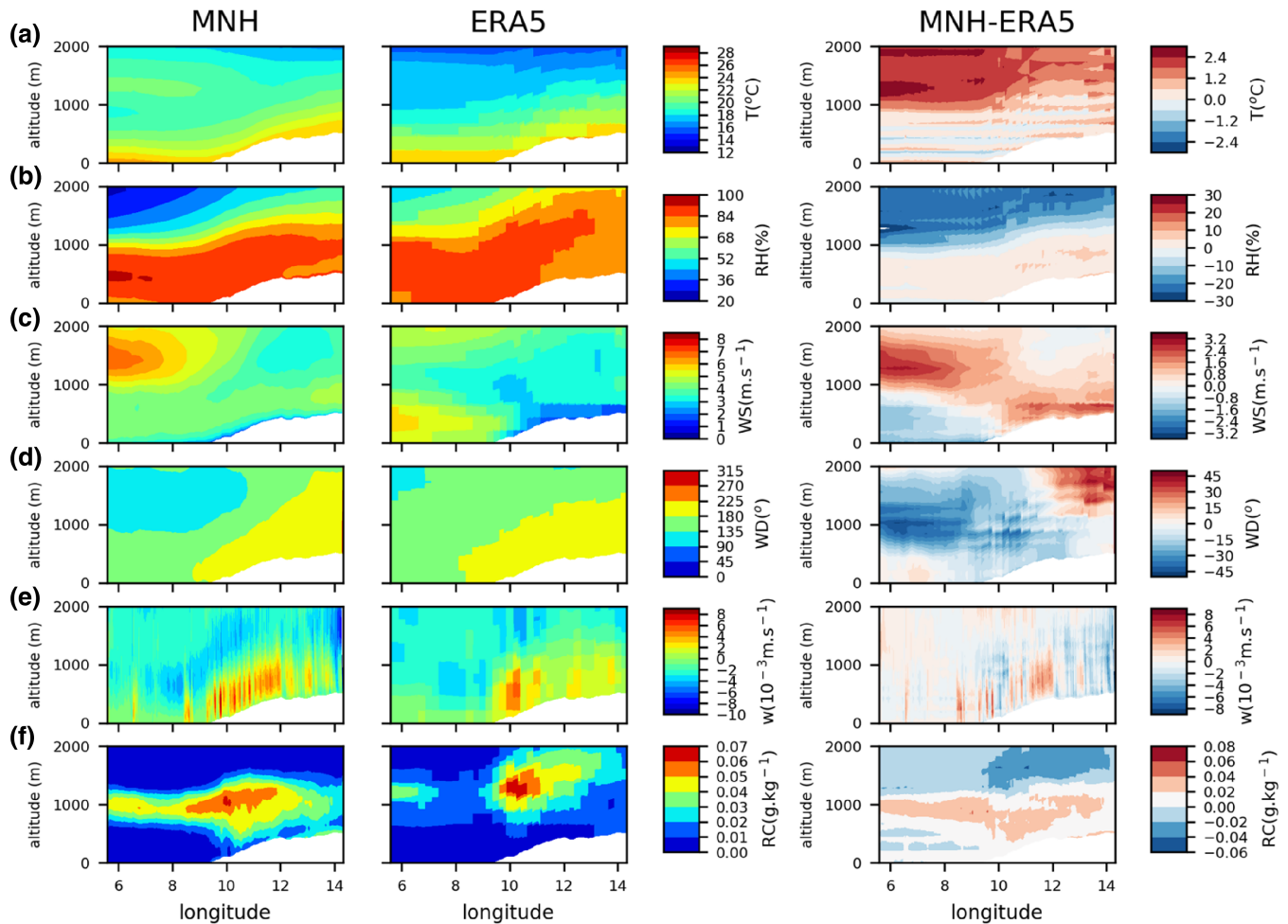


FIGURE 6 Longitudinal cross-sections of meteorological variables averaged all over the six-day period and the latitudes of domain 2 (5°S – 3°N) for Meso-NH and ERA5. (a) temperature (T , $^{\circ}\text{C}$); (b) relative humidity (RH , %); (c) wind speed (WS , m.s^{-1}), (d) wind direction (WD , degrees from north); (e) vertical velocity (w , m.s^{-1}); and (f) cloud mixing ratio (RC , g.kg^{-1}). White area represents the mean longitudinal cross-section of orography. [Colour figure can be viewed at wileyonlinelibrary.com]

at the latitude of the finer domain of the simulation (domain2).

A notable feature is the temperature inversion at about 1000–1500 meters above the Atlantic Ocean west of 10°E . The inversion is clearly visible in Meso-NH, contrary to ERA5, due to a warmer free troposphere (~ 1 – 2.5°C) above 1000 m (Figure 6a) in Meso-NH. As a result, above 1000 m from the ground, the free troposphere is drier ($\text{RH} < 70\%$) than below the boundary layer ($\text{RH} > 80\%$). However, the simulated free troposphere is drier (up to -30% in difference) than in ERA5, while in the boundary layer there is very little difference in humidity ($< 5\%$) (Figure 6b). The wind directions are very similar (Figure 6d): south-westerlies prevail over the continent (east of 10°E) below 1000 m, and are replaced by southeasterlies above. However, free tropospheric winds are slightly stronger (up to 2 m.s^{-1} more) in Meso-NH (Figure 6c). The pattern of the vertical velocity, w (Figure 6e), is broadly similar between

Meso-NH and ERA5 with upward flow in the boundary layer and downward flow above. However, Meso-NH simulates smaller convective cells as a result of the increased horizontal and vertical resolution. A distinct low-level peak in the cloud mixing ratio (Figure 6f) is found near the coast and slightly inland (around 10°E) in both datasets, but it is at a higher elevation in ERA5 (near 1200 meters) than in Meso-NH (near and below 1000 m). This suggests that both datasets produce a low-level cloud deck (thicker inland) but differing in the height of both the cloud base and cloud top.

3.3 | LCC variations in space and time

The last two subsections showed that the mean surface conditions simulated by Meso-NH only show moderate differences with ERA5. Larger differences are found

when considering temporal variations, especially for some variables such as wind speed and direction. Some discrepancies also exist between ERA5 and Meso-NH in the vertical structure of the lower troposphere. This might explain the differences in LCC, which are now examined more closely.

The mean diurnal LCC cycle is first analyzed (Figure 7). Since we are mainly interested in the presence/absence of a low-cloud deck, and its spatial extension, statistics are based on low-cloud frequencies across a network of seven stations, and the co-located grid point for gridded datasets. While satellite data directly provide binary results on LCC presence/absence, for the model, reanalysis and station data, the LCC presence/absence is based on cloud fractions. For station data, a cloudiness of at least four octas (0.5 LCF) is a standard assumption for LCC occurrence. To define LCC occurrence in Meso-NH and ERA5 data, we explore a range of LCF thresholds, given possible biases in the data. Additionally, as discussed in Section 2.5, there are different methods to compute LCF in models depending on overlap assumptions. To define the most appropriate method to use in the present study, Figure 7 compares the hourly mean frequency throughout the diurnal cycle of LCC occurrence computed from Meso-NH, using both maximum-random (in blue) and random-overlap (in orange) assumptions, to ERA5 (in green) and SYNOP observations (in black). The comparison between the two methods is justified by the transition from stratocumulus to cumulus in the afternoon.

Figure 7 displays boxplots, for each overlap assumption in Meso-NH data, and for ERA5, which depict the dispersion of low-cloud frequencies obtained for a range of LCF thresholds from 0.1 (sky 10% covered) to 1 (sky fully covered) by steps of 0.1. Blue, orange and green lines represent the LCF at a threshold of 0.5 for MNH and ERA5. For station data, both the stratiform-only (dashed black line on Figure 7) and the total low-cloud cover frequencies (solid black line) are provided. Only seven stations (in red on Figure 1) regularly report LCF and cloud genus at daytime over the region and period of observation and are thus used in the calculation, but caution should still be exerted as the number of stations in the computation slightly varies. The virtual absence of night-time observations prevents computing the index from 2100 to 0300 UTC.

SYNOPSIS data show that on average, close to 90% of the stations report low-level clouds (more than four octas) at 0600 UTC. The low-level stratiform cloud occurrence gradually decreases to a minimum of roughly 40% at 1500 UTC, then stabilizes. However, some cumuliform clouds develop in the afternoon, keeping the overall cloud frequency near 75%, until a quick drop to 45% at 1800 UTC. These daytime variations agree with those found over the South Atlantic Ocean by Painemal et al. (2015) and Seethala et al. (2018). The early-morning peak and the subsequent decrease is well matched by Meso-NH, though only if stratiform-only LCC are considered, suggesting some issues of Meso-NH in resolving the stratocumulus to cumulus transition in the afternoon. The method

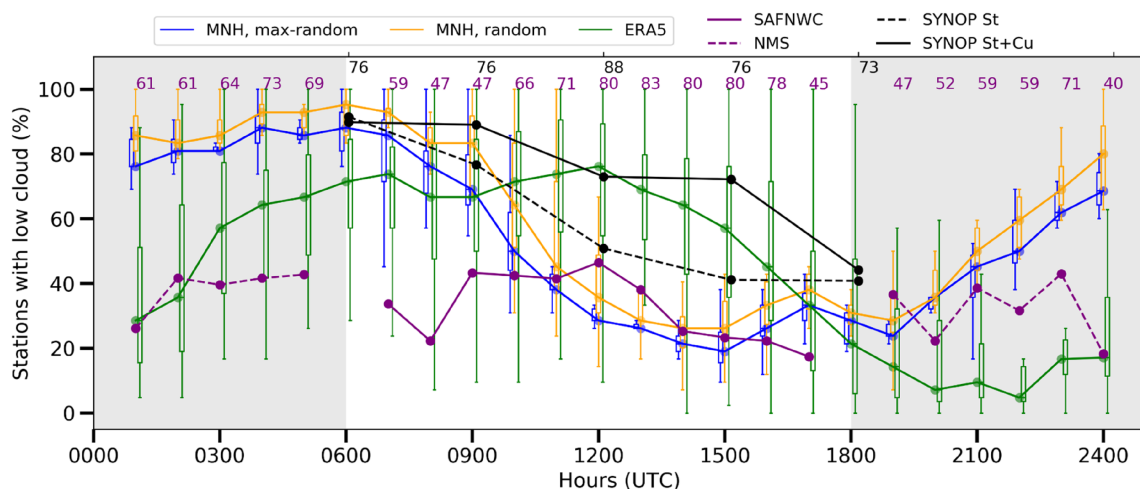


FIGURE 7 Mean diurnal cycle of low-level cloud frequency at seven SYNOP stations and at co-located pixels. SYNOPSIS frequencies are based on stratiform-only (dashed line) and all low-clouds data (solid line). ERA5 data are in green, and satellite data in purple (NMS [night microphysical scheme]: dashed, SAFNWC: solid). For Meso-NH, two different cloud assumptions are considered (maximum-random overlap in blue; random overlap in orange). The box plots show the distribution of the percentage of pixels with low-level clouds according to total LCC thresholds from 0.1 to 1.0 by steps of 0.1. The lines show the LCF at a threshold of 0.5 for MNH and ERA5. Numbers at the top correspond to the three-hourly percentage of data available for SYNOPSIS. Night-time SYNOPSIS data are not shown because of insufficient data availability. Purple numbers correspond to the hourly percentage of data available for NMS (0100–0500 and 1900–2400 UTC) and for SAFNWC (0700–1700 UTC). [Colour figure can be viewed at [wileyonlinelibrary.com](https://onlinelibrary.wiley.com/terms-and-conditions)]

used to compute LCC in Meso-NH has little impact on the results. The random-overlap method provides values slightly closer to synoptic observations, but the overall diurnal variations are similar, whatever the method. It should be noted that low-level cloud frequency is more sensitive to the LCF threshold than to the cloud overlap methods. ERA5 shows smaller low-level cloud frequencies than both the observed and Meso-NH data, except in the middle of the day. ERA5 has a 70% cloud frequency at 0600 UTC, lower than in SYNOP and Meso-NH. However, contrary to both observations and Meso-NH, ERA5 does not show any LCC decrease in the morning. Instead a LCC peak occurs at 1200 UTC before a decrease until 2200 UTC.

The ERA5 diurnal cycle is almost the same for the random-overlap and maximum-random-overlap assumptions (not shown). However, values obtained using the random-overlap assumption are closer to the ERA5 original 2D LCC field. Satellite data show moderate cloud frequencies (about 20% to 50%) throughout night and day. Though station data are lacking at night over the period of study, the satellite night estimates are quite dubious given the known LCC diurnal cycle in the region (Dommo et al., 2018, 2022; Champagne et al., 2023). In the early morning, the low frequencies obtained from SAFNWC satellite data are also questionable as they do not match SYNOP data, either with or without cumulus clouds.

Champagne et al. (2023) noted a LCF underestimation by satellite data over coastal Gabon, and their Figure 10 shows a large number of cloud-free satellite reports at times of stratocumulus (night-time) and cumulus (day-time) ground observations, for NMS and SAFNWC satellite data respectively (their Figures 10a and 10j). Van der Linden et al. (2015) also found some discrepancies among the satellite products in the reproduction of low clouds in SWA. Although SAFNWC generally well depicts the day-time low-cloud cover, it was found to underestimate the cloud occurrence frequency when compared with SYN-OPs, especially in the morning hours.

On the whole, the Meso-NH low-cloud frequencies and diurnal variations are quite realistic, except that cumuli-form clouds in the afternoon are underestimated. The different overlap methods do not have a major impact, but given its slightly better agreement with SYNOP, the random-overlap assumption will be retained in the subsequent analyses, with a LCF threshold of 0.5, that is, four octas, as applied for ground observations.

The LCC time evolution during the six-day period is described in more detail on Figure 8, which shows hourly variations in the three subdomains for Meso-NH and ERA5, compared to satellite observations.

The oceanic subdomain (subdomain 1; top panel) displays a low-level cloud frequency generally below 50% in ERA5. The satellite data also show relatively few

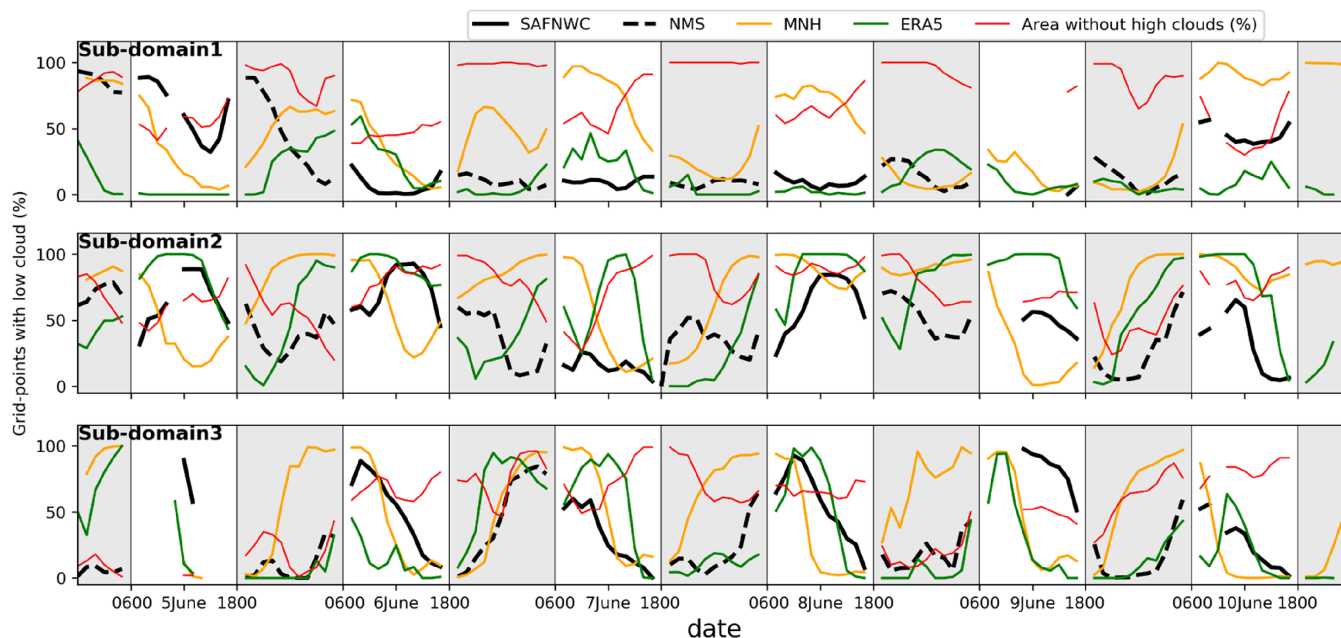


FIGURE 8 Mean hourly percentage of grid points with low-level cloud cover for SAFNWC (daytime, solid black lines), for night microphysical scheme (NMS) (night-time, dashed black lines), for Meso-NH (orange) and for ERA5 (green), over the three subdomains (1,2,3 from top to bottom). The percentage is calculated only on grid points in NMS and SAFNWC without high clouds. Red curves indicate the percentage of the grid points without high clouds in each subdomain. The LCF threshold to detect low-level cloud occurrence is 0.50 for both ERA5 and Meso-NH (random-overlap method). [Colour figure can be viewed at [wileyonlinelibrary.com](https://onlinelibrary.wiley.com/doi/10.1002/qj.4962)]

clouds, but the day-to-day variations are different, with more low-level clouds in the early and late parts of the period. Meso-NH has more low-level clouds compared to ERA5 and the satellite retrievals. Further, all LCCs have a variable diurnal cycle in amplitude. On the whole, the agreement between the three datasets is relatively poor over the ocean. While the presence of low-level clouds in ERA5 is sensitive to the threshold value, lowering the threshold only slightly impacts the amount but not the chronology (tested but not shown here) over subdomain1.

The continental subdomains (2 and 3) show a good agreement. Subdomain3 (the most inland one – Figure 8, bottom panel) exhibits the most regular diurnal cycle, with a recurrent late-night to early-morning peak in Meso-NH, then the low-level clouds dissipate in the afternoon. The highest LCC amount in ERA5 is later and weaker compared to the satellites as shown on Figure 8. By contrast, in Meso-NH the peak often comes earlier than in the satellite data. There are some discrepancies in LCC, for instance on the nights of 5–6 June and 8–9 June. They are partly related to the fact that high clouds obscure the lower layers in NMS (not shown here).

Closer to the coast in subdomain2 (Figure 8, middle panel), Meso-NH shows a diurnal pattern quite similar to that of subdomain3, with the peak cloudiness generally occurring near 0600 UTC, but the afternoon clearing is more uneven. For instance, the low-level clouds even remain present on 8 June during the whole day. This agrees with the climatological study by Champagne et al. (2023) which showed that the afternoon clearing was less frequent in subcostal areas than further inland. ERA5 again shows a delayed peak (in the late morning in general) and

delayed minimum cloudiness. The first part of the night is mostly cloud-free, while in Meso-NH the LCC formation starts earlier. Some discrepancies also affect the day-to-day variations, but the contrast between 7 June (reduced afternoon cloud cover) and 8 June (persistent low-level clouds) is prominent in both Meso-NH and ERA5. The agreement between the latter two datasets and the satellite data is therefore moderate to poor in this subdomain, but Meso-NH and ERA5 also quite often depart from each other.

On the whole, while there are many differences between the different datasets in both the temporal and spatial patterns of the LCC, some of them being related to the nature of the data and the way low-level clouds are detected, Meso-NH often shows more realistic features than ERA5, at least at daytime, which advocates for a further examination of the cloud patterns at station level. The time evolution from 5 to 10 June at an hourly or three-hourly time-scale (depending on the product) is shown on Figure 9, for the seven stations retained above and their co-located pixels. Note that as the pixels do not cover the same surface area in all the products (4 km² for Meso-NH, 9 km² for NMS and SAFNWC, 400 km² for ERA5), we have also tested to average the cloud occurrence over larger windows (not shown here). The time series are very close to those obtained for co-located pixels, which demonstrates the robustness of the results.

The average of the seven stations (Figure 9) shows that the decrease in observed low-level cloud from morning to afternoon, as noted above, is conspicuous almost every day. However, the afternoon minimum shows some variations, with an outstandingly very small low-level cloud

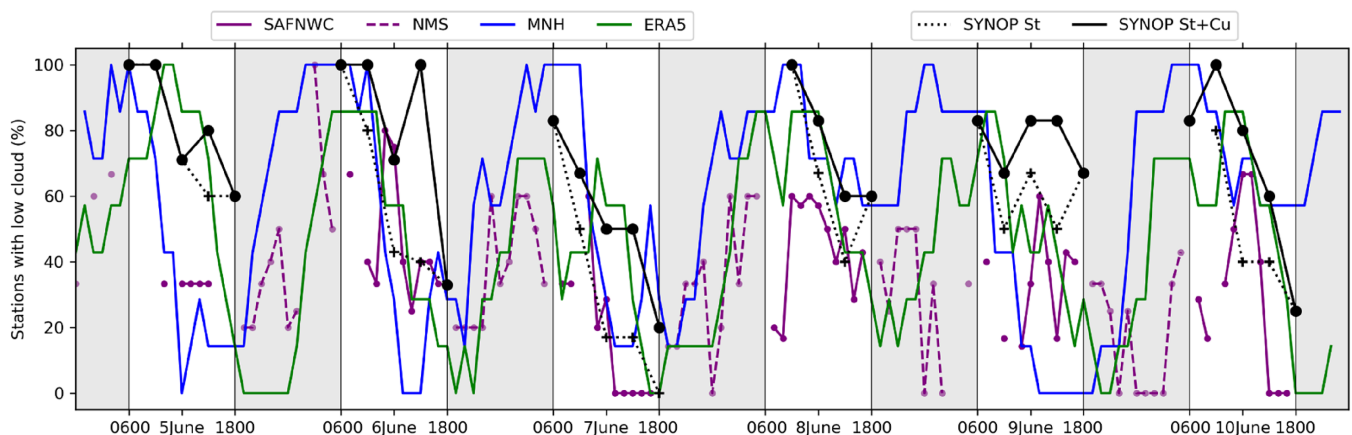


FIGURE 9 Hourly or three-hourly variations of low-level cloud frequency at the seven stations from 5 to 10 June 2008, as a percentage of stations or co-located grid points with a low-level cloud cover in SAFNWC (purple solid lines), NMS (night microphysical scheme; purple dashed lines), Meso-NH (blue), ERA5 (green) and SYNOP (black, solid for any low clouds and dashed for stratiform clouds). White bands denote daytime and gray bands night-time. The observed percentage of stations with low-level clouds is not computed when less than four stations are available. [Colour figure can be viewed at [wileyonlinelibrary.com](https://onlinelibrary.wiley.com/doi/10.1002/qj.4962)]

occurrence on 7 June. For the part of the day where synoptic data are available, Meso-NH matches observations, though the afternoon decrease is sometimes too strong. On 5, 6 and 9 June, the frequency of low-level clouds is down to 0%–20% in Meso-NH while 40%–60% of the synoptic stations still record stratiform low-level clouds. The agreement is better on 7 June (an almost cloud-free day), 8 and 10 June (both much more cloudy).

Satellite data show quite uneven variations which do not always match the Meso-NH, SYNOP and ERA5 variations. The cloud frequency is generally lower than all the other data, especially in the morning as reported above, which suggests that the satellite data need to be handled with caution. Similarly, on the nights of 8–9 and 9–10 June, the NMS data show very low values but their reliability is hampered by the frequent high clouds. However, the cloudless conditions in the afternoon of 7 June are confirmed, contrasting with much more cloudy conditions the following day.

A more detailed LCC analysis was made at station level. To that end, the cloud cover lifetime at six locations is pictured on Figure 10. The plots monitor the LCC vertical distribution (from the surface to 2200 m) in Meso-NH (red shadings) and ERA5 (blue shadings). At Libreville on the coast in northwestern Gabon (Figure 10a), SYNOP data show long periods of overcast skies (6–8 octas – red and blue values at the bottom of panel a) associated with stratiform clouds (“S” at the top of the panel). The interaction between the low-level circulation and the coastal hills may explain these persistent cloudy spells. They are interrupted, generally in the afternoon, by broken, often convective clouds (“C”). Meso-NH unevenly replicates these LCC variations. For instance, on 8 June Meso-NH shows cloudy conditions the whole day, whereas ground and satellite data reveal a partial clearing in the afternoon and evening. However, the extensive clearing on 9 June is well reproduced. The cloud base in Meso-NH is found at a very low level (often around 200 m in Meso-NH), in agreement with the SYNOP observations, and lower than in ERA5. The stratiform cloud top reaches about 1000 m, which is lower than in ERA5.

At Makokou (Figure 10b), over 300 km inland (subdomain3), low-level clouds are again very persistent but often turn from stratiform into cumuliform in the afternoon. Satellite data show frequent high clouds (some of them likely of convective nature) and are therefore of limited use to monitor low-level clouds. Meso-NH displays a recurrent night-time setup of low-level clouds. In ERA5, this is less consistent, and there is a delay in the formation. The cloud deck is at a slightly higher elevation at Makokou than at the coast, except for occasional morning stratus near the ground in Meso-NH (8 and 10 June).

Port-Gentil (Figure 10c), on Cape Lopez, which protrudes into the ocean with no coastal hills, contrary to Libreville, has quite distinct low-level cloud variations. The low-level clouds simulated by Meso-NH are frequent but quite shallow. Both the ground observations and the satellite data show that low-level clouds are much less frequent than at any other location, in agreement with what was found over the Atlantic Ocean (Figures 7 and 8).

The last three stations (Lambaréné, Tchibanga and Pointe-Noire – Figure 10d–f), located along or relatively near the coast (subdomain2) in the southern half of the subdomain, share a similar low-level cloud behavior. In Meso-NH, on most days, a LCC develops in the middle of the night at low elevations, then thickens and rises to about 1000 m, before partly or completely clearing in the afternoon. ERA5 shows similar but later cloud cover changes, and a faster elevation rise. In the second half of the period, the late-night clouds tend to have an ultralow base. Observed day-to-day changes are fairly well reproduced by Meso-NH. For instance the marked afternoon clearing on 7 June coincides with a cloud break-up in SYNOP observations, whereas on 8 June the simulated persistence of the cloud cover agrees with observations (5–8 octas).

Before analyzing the mechanisms associated with LCC variations, a brief summary is provided of the accuracy of Meso-NH simulations in simulating both standard meteorological variables and the LCC, as depicted from Sections 3.1 to 3.3. Firstly, the comparison of surface meteorological variables (T2, RH2, WS10 and WD10) at synoptic stations indicates a good overall performance of Meso-NH, although Meso-NH underestimates T2 and WS10, and simulates a stronger southerly wind compared to observations. Secondly, at subdomain scale, the performance of Meso-NH is similar to that of ERA5 with a diurnal cycle in phase and with the same intensity for most variables. The greatest discrepancies are for the lower-tropospheric RC for which Meso-NH simulates a stronger diurnal cycle than ERA5 mostly over subdomains 2 and 3. Moreover, the mean longitudinal cross-sections of these meteorological variables show discrepancies in the boundary layer mostly for w and RH, which are higher in Meso-NH than in ERA5, and wind speed which is lower above the ocean and weaker above land in Meso-NH. Above 1000 m, T is higher and RH is lower in Meso-NH. These differences probably explain the lower LCC elevation in Meso-NH (around 1000 m) than in ERA5 (around 1300 m). Thirdly, the station-by-grid point analysis of LCC variations in space and time show that, on the whole, Meso-NH simulations reasonably replicate LCC ground observations. The diurnal cycle of LCC at synoptic stations is well captured by Meso-NH, with a more realistic phase

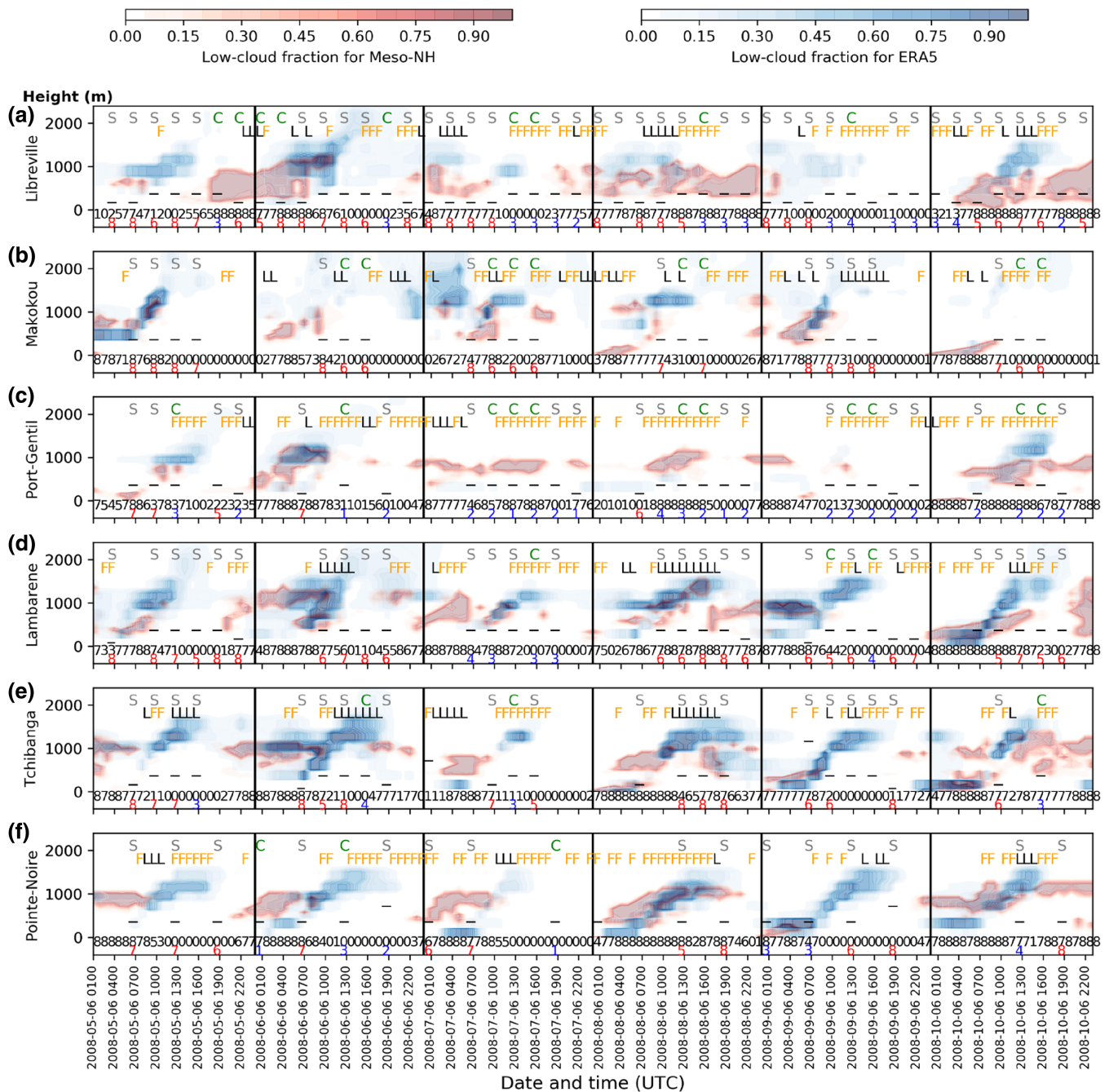


FIGURE 10 Time × height diagrams (0 to 2200 m above ground level) of hourly cloud fraction for Meso-NH (red shadings) and ERA5 (blue shadings) at six stations from 5 to 10 June 2008. Red numbers from 0 to 8 indicate observed cloudiness in octas, with the type of clouds indicated on top (S, stratiform cloud; C, cumuliiform cloud). Black numbers from 0 to 8 indicate Meso-NH cloudiness in octas. Black and orange letters show available satellite information (L, low cloud; F, clear sky). “_” indicates the height of the cloud base from SYNOP reports. [Colour figure can be viewed at wileyonlinelibrary.com]

locking than in ERA5. Some form of geographical coherence in the low-level cloud formation, dissipation and elevation, is also revealed, with different patterns from south to north and from the coast to the interior. Although it must be emphasized that there is no perfect reference data to document LCC, we find that Meso-NH does a good job in the overall simulation of low-level clouds.

3.4 | Mechanisms of LCC formation

In this section, we shed light on the atmospheric changes which may account for the LCC space–time variations. Given the contrasted patterns found on 7, 8 and 9 June in the afternoon (very cloudy on 8 June, less cloudy on 7 and 9 June), and the relative consistency between Meso-NH

simulations, ground-based and satellite observations for these three days, the following analyses are first restricted to this three-day period, then a broader view is provided.

To document the origin of the persistent LCC observed on the afternoon of 8 June, Figure 11 displays longitudinal cross-sections (averaged over 0° – 5° S, i.e. including the subdomains 1 and 2) of selected variables averaged between 1500 and 1700 UTC for each day from 7 to 9 June. The cloud mixing ratio (RC) clearly shows the persistence of a LCC around 1000 m high over both the ocean (west of about 10° E) and land on the afternoon of 8 June, and over the ocean only, far offshore, on the afternoon of 7 June. No LCC is found on the afternoon of 9 June. For the three cases, there is a strong vertical gradient of vapor mixing ratio (RV) with moist air ($>14 \text{ g}\cdot\text{kg}^{-1}$) in the lowest 600 to 1000 m, and much drier air above (minimum of about $1\text{--}3 \text{ g}\cdot\text{kg}^{-1}$ around 2000 m), mostly over the ocean. However, over the ocean the moist boundary layer is thinner on 9 June than on the other two days. Very dry mid-tropospheric air also prevails over land on 9 June, compared to the previous days. Moreover, the wind direction (central panels) varies greatly depending on the day, longitude and height. Between 500 m and 1000 m high,

the wind blows from the southeast and northeast on 7 and 9 June, respectively, while it blows from the southwest (onshore) on 8 June. In the layer between 1000 m and 2000 m, a well-established easterly circulation occurs on 7 and 9 June inland, while the winds are weak and subsiding on 8 June. Above this layer, a westerly subsiding flow is also found on 8 June. Offshore, subsiding wind prevents in-cloud mixing at the top of the PBL and maintains the LCC for 7 and 8 June. Moreover, it is found for the three days that the PBLH (black lines, left panels) is lower when approaching the coast, probably as a result of the low coastal sea surface temperature (SST; not shown) which stabilizes the atmosphere.

Over land, the change in the low-level wind direction has a clear effect on the LTS (black lines, right panels). On 8 June, the wind comes from the southwest bringing cooler air toward coastal lands thus increasing stability in the lowest layers. This leads to a LTS maximum near $10.5\text{--}11^{\circ}$ E, whereas for 7 and 9 June the maximum is located offshore near 9.5° E. On 8 June, the LCC is therefore present both offshore (west of 10° E) and onshore (10° E– 12° E) with a maximum thickness over the first hills before dissipating inland (east of 12.5° E).

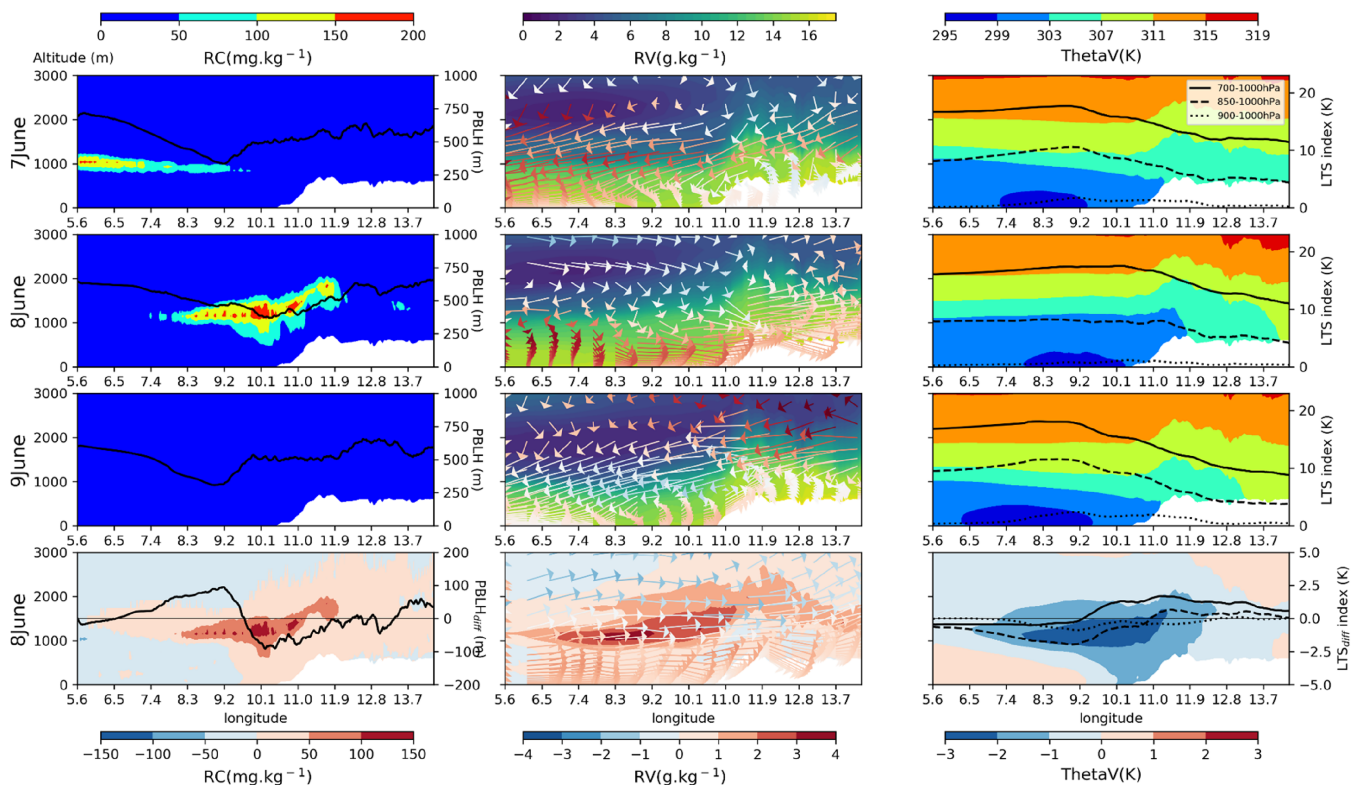


FIGURE 11 Top: Longitude \times height (0–3000 m) cross-sections for several Meso-NH fields for 7, 8 and 9 June 2008 averaged between 1500 and 1700 UTC and over latitudes 5° S– 0° . Left panels: cloud mixing ratio (RC, shadings) and planetary boundary layer height (PBLH; black line; right scale, 0–1000 m). Central panels: relative velocity (RV) and wind direction (zonal and vertical components, with blue showing northerlies and red southerlies; vertical component is multiplied by 100). Right panels: virtual potential temperature (ThetaV) (shadings) and low-troposphere stability (LTS) indices (700, 850 and 900 hPa minus 1000 hPa ThetaV, respectively) (black lines). Bottom, differences between 8 June and the 7–9 June mean. [Colour figure can be viewed at wileyonlinelibrary.com]

The differences ($_{\text{diff}}$) between 8 June and the mean atmospheric conditions over this three-day period (bottom panels of Figure 11) highlight well an enhanced stability over the coastal lands on 8 June ($\text{PBLH}_{\text{diff}} < 0$, $\text{LTS700}_{\text{diff}}$ and $\text{LTS850}_{\text{diff}} > 0$), caused by advection of colder air from the ocean ($\text{ThetaV}_{\text{diff}} < 0$), driven by westerly winds. Also, the lower troposphere (up to 2000 m high) is moister on 8 June compared to the three-day average. Thus, these cross-sections highlight the key role of the wind direction

over the region influencing humidity, cooling and stability in the PBL and at the origin of the LCC formation.

A further exploration of the causes of the persistent LCC over coastal lands on the afternoon of 8 June requires an analysis of the diurnal variations. Figure 12 shows time–height diagrams at the hourly time-scale averaged over subdomain2.

On 7 June, the LCC forms from midnight below 1000 m height above the ground with a maximum cloud

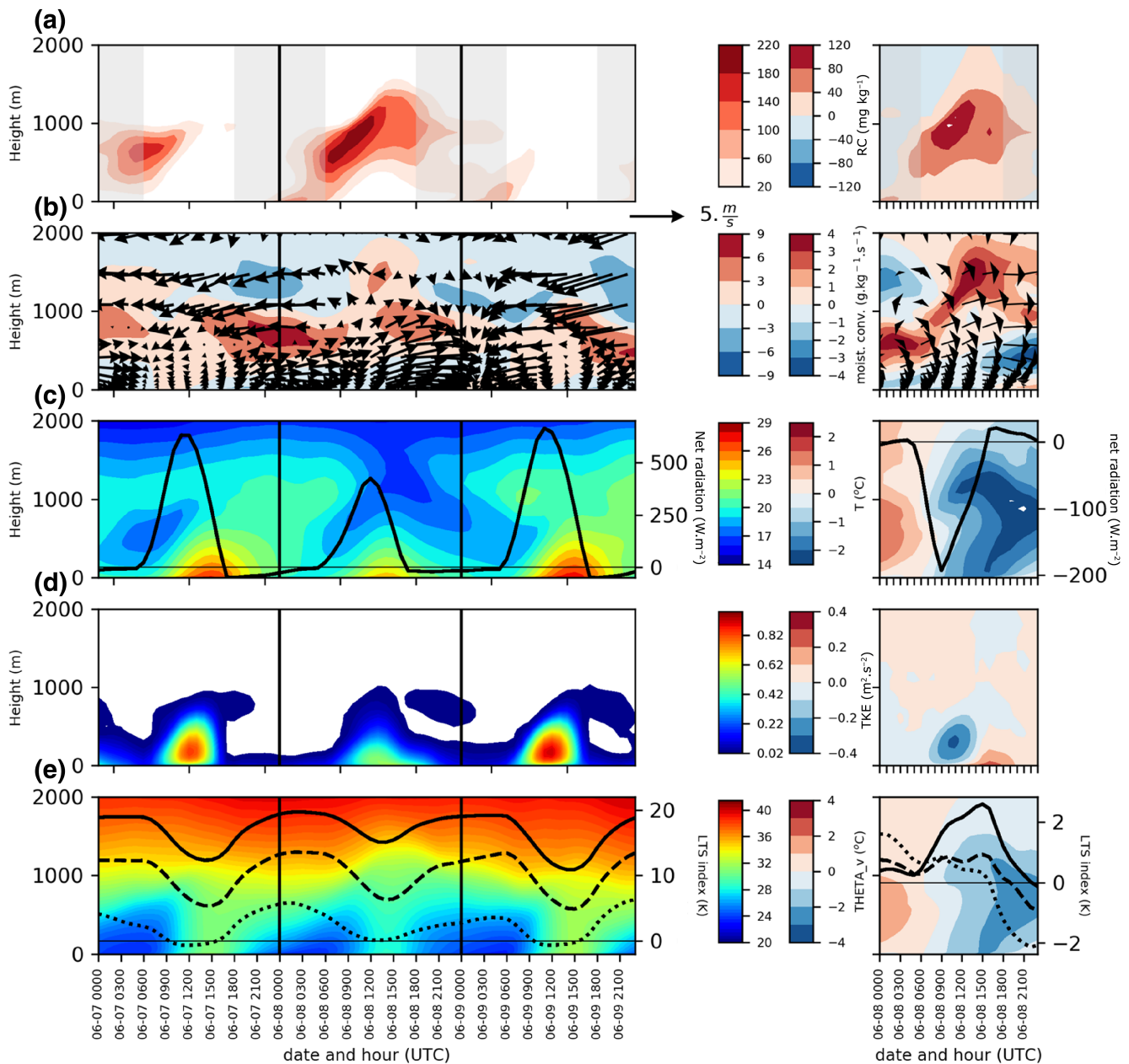


FIGURE 12 Hourly time-scale time–height diagrams over subdomain 2 from 7 to 9 June (left panels), and differences between 8 June and the three-day average (right panels) for several Meso-NH fields. From top to bottom: (a) cloud mixing ratio (RC , $\text{g}\cdot\text{kg}^{-1}$), (b) moisture convergence ($\text{g}\cdot\text{kg}^{-1}\cdot\text{s}^{-1}$) and wind direction (zonal and vertical components $\times 100$) represented by arrow direction), (c) temperature ($^{\circ}\text{C}$) and surface net radiation ($\text{W}\cdot\text{m}^{-2}$), (d) turbulent kinetic energy (TKE , $\text{m}^2\cdot\text{s}^{-2}$), (e) virtual potential temperature ($^{\circ}\text{C}$, shadings) and low tropospheric stability indexes at 700 hPa (LTS700 , solid), 850 hPa (LTS850 , dashed) and 900 hPa (LTS900 , dotted). [Colour figure can be viewed at wileyonlinelibrary.com]

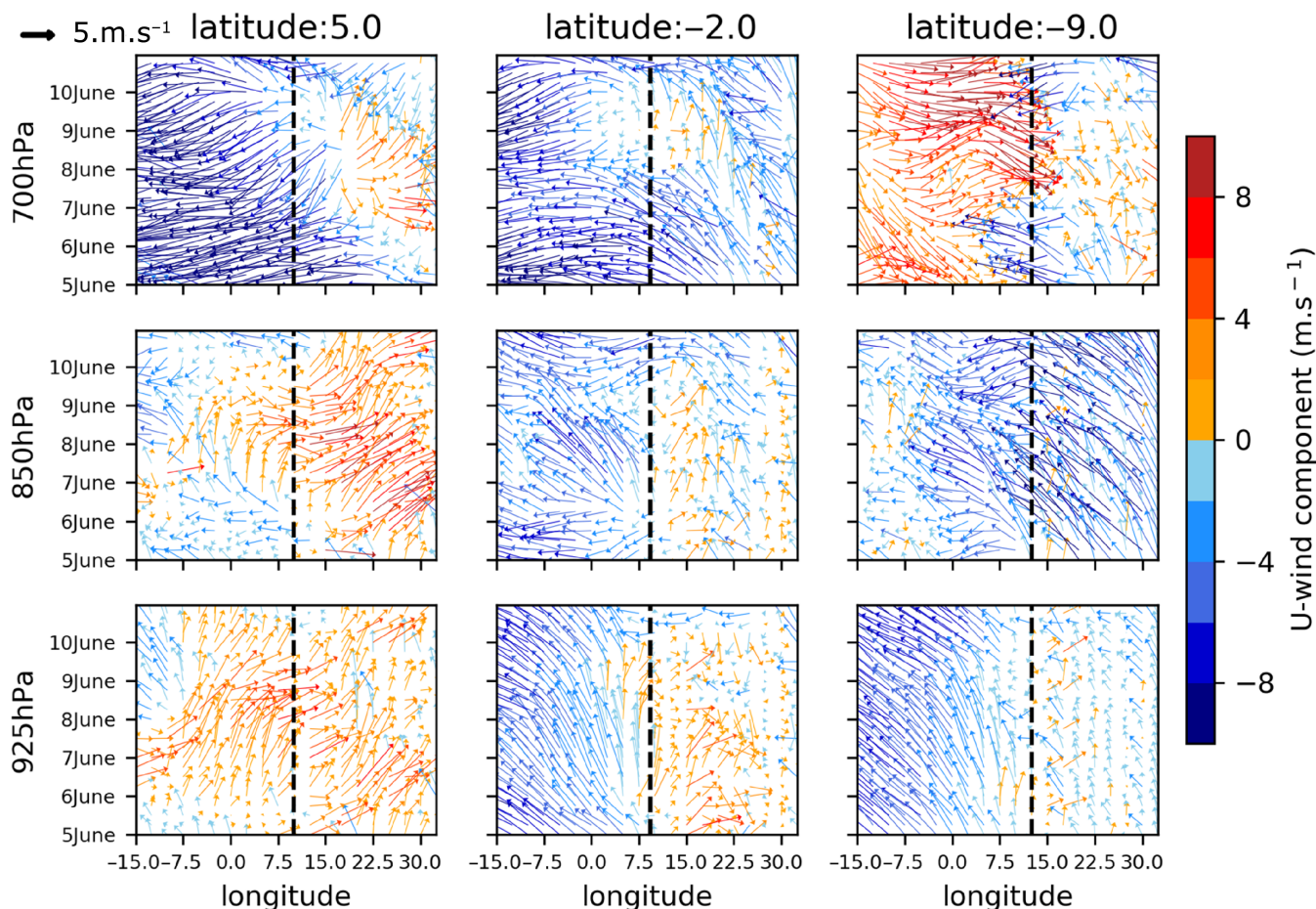


FIGURE 13 Longitudinal Hovmöller diagram (every 6 h) of ERA5 horizontal wind at 700 hPa (top), 850 hPa (middle) and 925 hPa (bottom) at three latitudes (5° N, 2° S and 9° S), from 5 to 10 June (y-axes). In blue and red, when the U-wind component is negative and positive, respectively. The dashed line shows the longitude of the coast. [Colour figure can be viewed at [wileyonlinelibrary.com](https://onlinelibrary.wiley.com/doi/10.1002/qj.4962)]

mixing ratio at the end of the night (Figure 12a). The low-level southwesterlies, which have blown since the end of the day before, bring cool air and moisture between heights of 500 and 1000 m from the ocean into the PBL as shown by the moisture convergence and the temperature (Figure 12b,c). Besides, positive LTS900 and low values of TKE (Figure 12d,e) show that the air mass is stable below 1000 m high. Thus, fog or very low clouds develop in the early morning. At 0700 UTC, the LCC is the thickest (RC between 140 and 180 $\text{mg}\cdot\text{kg}^{-1}$, Figure 12a) and the southwesterly wind weakens. Then, the sunlight warms up the ground (surface net radiation increases, Figure 12c) and the PBL thickens (TKE increasing). From 0900 UTC, the air becomes unstable ($\text{LTS} < 0 \text{ m}^2\cdot\text{s}^{-2}$, Figure 12e), the air in the PBL is mixing (TKE increasing, Figure 12d), the cloud deck rises and a stratocumulus to cumulus transition sets in before a total LCC break-up before 1200 UTC (Figure 12a). At 1200 UTC, the sky is clear and surface net radiation is maximum ($600 \text{ W}\cdot\text{m}^{-2}$). At 1500 UTC, surface air temperature and buoyant TKE production are maximal and the PBL is still unstable. The vertical mixing of

atmospheric layers is the strongest. At 1800 UTC, the westerly flow revives and the sun sets which cools the PBL and stabilizes it. Above 700 m from the ground, the wind blows from the northeast and the air warms from 18°C to 20°C .

On 8 June at 0000 UTC, fog and LCC develop (Figure 12a) because of the strengthened low-level inversion (increased LTS900 index) and thanks to a strong moisture convergence (Figure 12b). At sunrise, the LCC is thicker than the day before (RC between 180 and 220 $\text{mg}\cdot\text{kg}^{-1}$) and surface net radiation (Figure 12c) shows that sunlight warms the ground less than on 7 June. The buoyant TKE production is weaker (Figure 12d) limiting the air mixing within the cloud layer. Contrary to the day before, the surface westerlies persist (Figure 12b). A concomitant feature is the collapse of the easterlies in the layer from 1000 to 2000 m. The absence of the (relatively warm) easterlies above the cloud deck and the advection of cool maritime air by the surface westerlies contribute to the persistence of the cloud deck. At 1200 UTC, the LCC is more dense (Figure 12a) than on 7 June and surface net radiation is lower ($400 \text{ W}\cdot\text{m}^{-2}$). The westerly wind

strengthens and, passing over low SST, cools the PBL air and promotes an inversion that inhibits entrainment and weakens in-cloud convection. The cloud deck slightly rises as a result of the (weak) surface heating and the orographic lifting of the surface airflow above the local hills. After 1600 UTC, the cloud ceiling lowers with the establishment of subsiding wind. A decoupling happens with a residual cell around 800 m high and another cell near the ground. Between 1800 and 0000 UTC, two cloudy layers form distinctly.

On 9 June, the westerly wind established on 8 June stops and in the morning easterlies blow not only above 800 m (as on 7 June) but also near the ground. Thus, the LCC formed at the end of the night as fog (near the ground), as a result of the thermal inversion, dissipates before 1200 UTC due to a dry and windy air. In the afternoon, the local meteorological conditions approach those of 7 June with a subsiding easterly wind above 800 m high and a weak westerly flow in the PBL.

The differences in lower-tropospheric conditions between 8 June and the three-day mean (Figure 12, right panels) emphasize the colder and more stable air mass on 8 June from 0000 to 1500 UTC and the change in the zonal wind flow. Another interesting feature is the moister air

found on 8 June in the upper part of the cloud deck and above it. It is hypothesized that it is due to the reduced subsidence associated with the collapse of the easterlies above 1000 m. This moistening may also contribute to the maintenance of the LCC. Thus, in the case of 8 June, it is suggested that the absence of LCC clearing in the afternoon is mainly due to surface westerlies advecting moister air from the ocean. The last two figures indicate that the main parameter that controls LCC formation is the wind direction because it directly influences the temperature at the surface and/or at the top of the PBL, and so controls the atmospheric stability. It is therefore essential to assess what is at the origin of the change of the local wind direction by considering large-scale atmospheric dynamics and a broader time window.

To do so, Hovmöller time–longitude diagrams of ERA5 winds at 700, 850 and 925 hPa are plotted for the latitudes 5° N, 2° S and 9° S (Figure 13), over the six-day period from 5 to 10 June. Although at the local scale ERA5 and Meso-NH show some differences in the LCC dynamics, ERA5, as the driving model and covering a larger area, is adequate to depict the large-scale (synoptic) wind flow.

North of the equator (5° N, Figure 13 left panels), the 850 hPa level shows winds predominantly from the

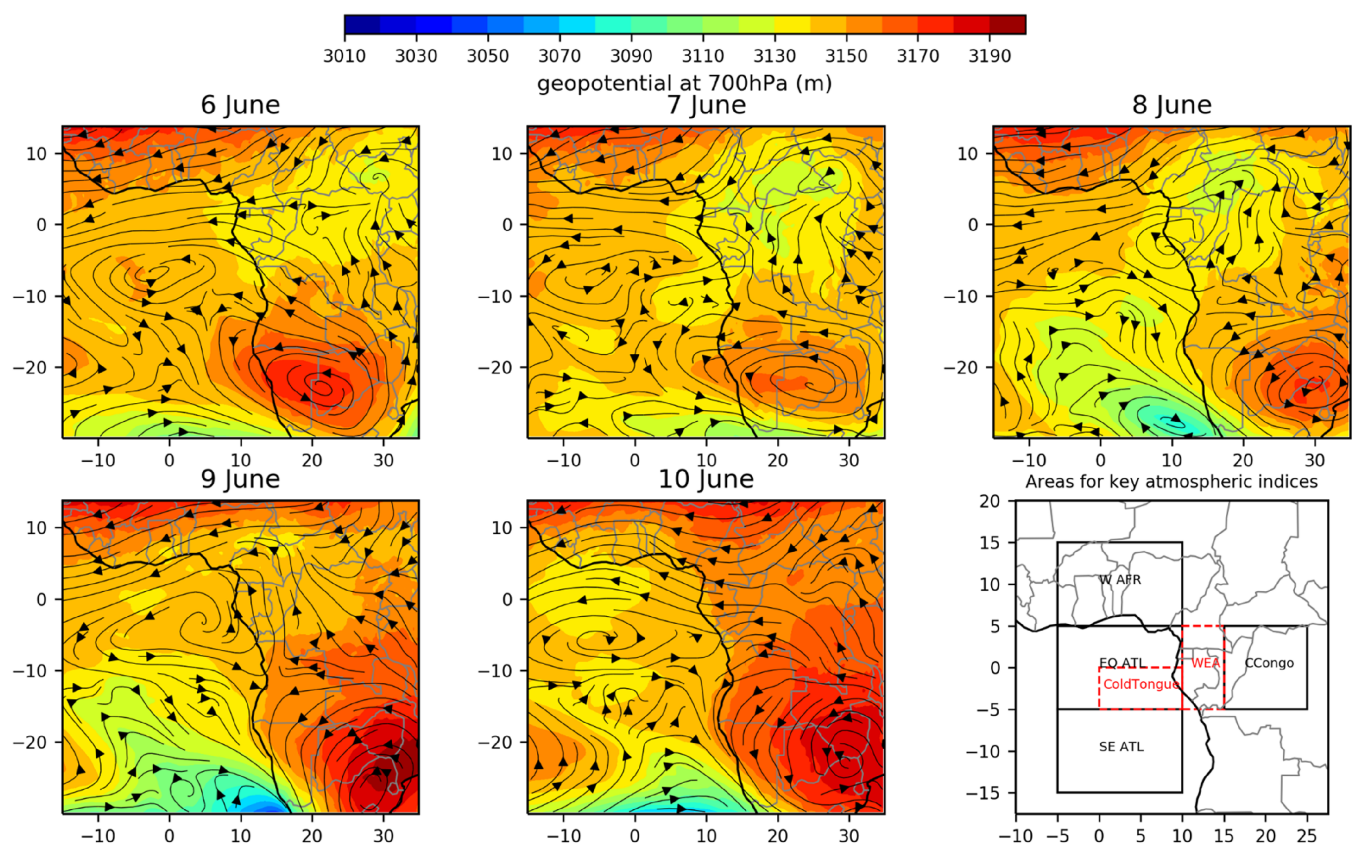
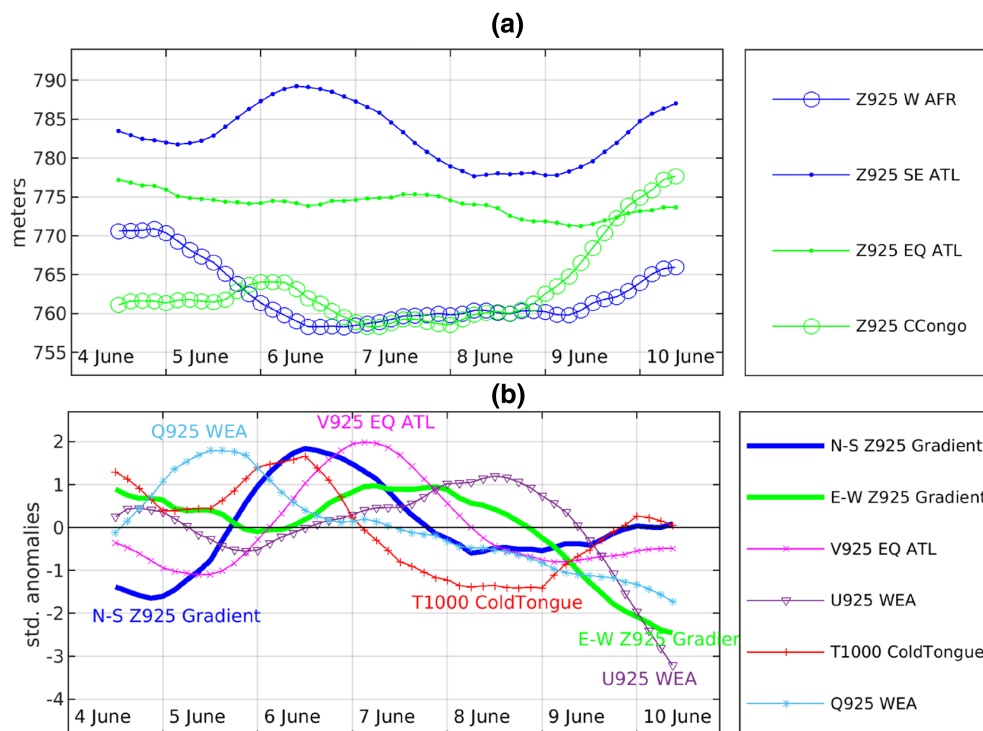


FIGURE 14 Streamfunction of horizontal wind and geopotential height at 700 hPa for 6, 7, 8, 9 and 10 June 2008 at 1600 UTC from ERA5 fields. Bottom right: areas for the computation of atmospheric indices used in Figure 15. [Colour figure can be viewed at [wileyonlinelibrary.com](https://onlinelibrary.wiley.com)]

FIGURE 15 Variations of ERA5 regional atmospheric indices from 4 to 10 June 2008: (a) 925 hPa geopotential heights; (b) standardized anomalies of lower-tropospheric atmospheric indices over the key regions shown on Figure 14. All values are sliding 24-h averages. [Colour figure can be viewed at wileyonlinelibrary.com]



southwestern quadrant over land. Offshore ($0\text{--}9^\circ\text{E}$), weak easterlies are replaced by westerlies around 8 June. This coincides with stronger southwesterlies to westerlies at 925 hPa. At 700 hPa, there is evidence of wave-like, westward-propagating signals, as shown by easterlies gradually receding, shifting westward between 25°E and the coastline from 5 to 9 June. The general easterly flow at this level (blue colors on Figure 13) is interrupted by a spell of westerlies propagating westward from the eastern Congo Basin. At 925 hPa (Figure 14 bottom) the southwesterly flow is more permanent, but the westward-propagating signal is also shown from 6 to 9 June in the form of strengthened winds.

At 2°S (Figure 13, middle column), the evidence of propagating signals is weaker, although at 700 hPa slackening southeasterlies propagate from east to west between 5 and 9 June, following the northern-hemisphere wave. At 925 hPa, westerlies briefly develop along the coast around 8 June, but the wind field further east or west undergoes little consistent changes. South of the domain (9°S , Figure 13 right panels), while little change also occurs at 925 and 850 hPa, more conspicuous signals are found at 700 hPa, where along the coast southeasterlies (5–6 June) are replaced by persistent westerlies from 7 June.

In order to better document the westward-propagating signal found at 5°N and the change in the mid-tropospheric wind direction in the southern hemisphere, maps of the 700-hPa streamlines and geopotential heights from 6 to 10 June are displayed on Figure 14.

North of the equator, a trough associated with a shear line between northeasterlies and southerlies is found near South Sudan on 6 June and gradually shifts westwards. It is located northeast of Gabon on 8 June. This feature is characteristic of an easterly wave (Parker & Diop-Kane, 2017; Poan et al., 2015). The passage of the easterly wave to the north of the equator results in a change in the wind flow above WEA. On 6 June, the southeasterlies originating from the Kalahari High over southern Africa ($20\text{--}25^\circ\text{S}$) converge with northeasterlies from the Sahel region (southern flank of the northern African Easterly Jet). On 7–8 June, the arrival of the trough over WEA disrupts the easterlies, which are replaced by southerlies. The easterlies resume on 10 June as the trough is replaced by a ridge around 15°E .

The maps also show changes in the southern hemisphere. From 6 to 9 June (Figure 14) there is a gradual eastward shift of the Kalahari High. As underlined above, this results in weaker southeasterlies on its northern flank (i.e., a reduced southern African Easterly Jet). Along the Atlantic Coast, these receding southeasterlies converge with westerlies / northwesterlies as a trough develops over the southeastern Atlantic Ocean (8–9 June). The western flank of the Kalahari High ultimately reinforces on 10 June, contributing to the resumption of the easterlies over WEA. The changes in the mid-tropospheric winds above WEA have a modest effect on moisture and temperature (easterlies tend to bring moister and warmer air from the Congo Basin), but they have a role in fixing the PBL height, which rises when they weaken.

Low-level dynamics also contribute to explain the LCC changes. Figure 15 shows the variations of key atmospheric indices at 925 hPa in the sequence from 4 to 10 June. From 4 to 6 June, there is a strong increase in the interhemispheric geopotential height gradient (pressure drop over West Africa and strengthening of the Saint-Helena High, Figure 15a). This results in a strong southerly monsoon flow over equatorial Atlantic (a day behind pressure changes – Figure 15b). The pressure gradient weakens on 7 June, which subsequently reduces the transequatorial flow from 8 June. In the meantime, consistently low pressure anomalies over the Congo Basin determine an east–west pressure gradient which drives sustained westerlies over WEA. These westerlies eventually collapse on 10 June as the pressure rises over the Congo Basin. Importantly, the very strong southerly flow around 7 June drives a cooling of the maritime boundary layer as denoted by the 1000 hPa temperature drop above the cold tongue area. On 8 June, associated with the enhanced low-level westerlies over WEA, this contributes to inland cold air advection.

On the whole, these results point to the complex interplay between lower- and mid-tropospheric dynamics in explaining LCC variations over WEA. It is hypothesized that the weakened easterlies (which bring warm and relatively moist air above the top of the boundary layer) tend to reduce LTS, paving the way for more clear conditions (7 June). The lower-tropospheric zonal pressure gradient, associated with a stronger temperature gradient between the warmer Congo Basin and the cooler southern Atlantic, in the absence of any strong upper easterlies, drives low-level westerlies, which bring a colder air mass, hence the transient setup of LCC after the relatively bright spell of 7 June. It is found that synoptic conditions in both hemispheres contribute to explain the atmospheric circulation changes over WEA, through variations in both the transequatorial flow and the mid-tropospheric winds, which depend on the shifts of the Kalahari High and the passage of easterly waves north of the equator. The east–west temperature and pressure variations in the lower troposphere along the equator also play a key role. As shown in the Meso-NH simulations, these dynamics interplay with the diurnal cycle resulting in either a daytime clear-up or a persistence of the LCC over WEA.

4 | CONCLUSIONS

The ability of the Meso-NH mesoscale model to simulate WEA dry-season conditions was examined over a six-day period in June 2008, characteristic of the early part of the cloudy season. This period has been chosen for its

changing cloudy conditions. The model was forced by ERA5 reanalysis data.

Key meteorological variables from MNH generally agree with ERA5 over WEA with the exception of the cloud mixing ratio showing a quite large RMSE over the three selected subdomains. This suggests a substantial difference in both spatial and temporal patterns that may result in partly dissimilar LCC dynamics between ERA5 and Meso-NH. The low-level temperature inversion around 1000 m which is a characteristic of this season is well reproduced in Meso-NH but its strength is slightly stronger than in ERA5, and the overlying free troposphere is drier.

Across the period of study there are significant variations of dynamical variables over the region, with a good agreement between ERA5 and Meso-NH over the ocean, including a pronounced weakening of the southeasterly trade winds from 6 to 8 June. Over land, there are more discrepancies between ERA5 and Meso-NH in the variations of wind speed, wind direction and cloud mixing ratio. However, the mean diurnal cycles at reference synoptic stations are well reproduced by both ERA5 and Meso-NH for a majority of variables.

The mean daytime variations of the LCC, as described by cloudiness reports at synoptic stations, are better reproduced by Meso-NH than by ERA5. This result does not depend on methodological issues such as the cloud overlap assumption or the LCF threshold retained to define cloudy observations. Meso-NH adequately simulates an early-morning maximum (low-level cloud occurrence ~90%), followed by a gradual decline toward the late afternoon (~40%), while in ERA5 the maximum is delayed toward noon. However, Meso-NH does not produce enough cumulus clouds in the afternoon after the break-up of the stratiform cloud deck.

More balanced results are obtained when the simulated cloud cover is compared to satellite data, but the latter struggle to identify low clouds, as demonstrated from a comparison with ground observations, and from the data published in van der Linden et al. (2015) and Champagne et al. (2023). Night-time cloud cover variations are particularly challenging to assess, with little ground observations as reference, and much uncertainty on satellite data. On the whole, ERA5 tends to show lesser amplitude day-to-day variations than both observations and Meso-NH. Over the ocean, where satellite data suggest that low-level clouds are less frequent than over land, Meso-NH overestimates the cloud cover, while ERA5 underestimates it. Over land, Meso-NH enables the depiction of subregionally coherent LCC dynamics, with different patterns from south to north and from the coast to the interior, in relatively good agreement with observations, though discrepancies often occur on individual days.

A thorough examination of three successive days with contrasting LCC (7 and 9 June with relatively clear afternoons, and 8 June with a persistent cloud cover) highlights the key role of the wind direction changes over WEA, resulting in more or less humidity, cooling and stability in the PBL. On 8 June, the absence of any low-level cloud clearing is associated with surface westerlies advecting cooler maritime air. This results in an increase in lower-tropospheric stability. High humidity is located above the PBL and not only in the PBL itself.

Three synoptic-scale features drive the local changes: (i) a mid-tropospheric easterly wave moving from the northern Congo Basin to western Africa between 6 and 9 June result in a disruption of the 700-hPa easterlies over WEA, which enables the PBL height to raise; (ii) a weakening of the Kalahari High over southern Africa also contributes to the demise of the mid-tropospheric easterlies and their replacement by westerlies; (iii) near the surface, as a result of a reduced interhemispheric pressure gradient, the weakening of the transequatorial flow (which earlier contributed to cool the equatorial Atlantic waters) results in the development of more onshore winds (southwesterly) over WEA, shown to be instrumental in the afternoon maintenance of low-level clouds on 8 June.

Several of these features were also shown to be instrumental in the statistical analysis of daily LCC variations carried out by Moron et al. (2025). In particular, the intensity of the low-level westerlies was found to be controlled by the Congo-to-Atlantic-Ocean geopotential height gradient, as in the June 2008 case study. Also in agreement with the present case study, enhanced southerly winds over the southeastern Atlantic Ocean have a cooling effect in the Benguela area which contributes, with a few days lag, to the advection of cold air, instrumental in the LCC increase, though the location of the pivotal areas is slightly different. Some triggers identified in June 2008, like the possible role of a northern-hemisphere easterly wave, do not emerge in the statistical analysis, but the event under scrutiny occurred in the early dry season and may not be fully representative of other events, and Moron et al. (2025) insisted on the variety of mechanisms operating at different time scales to explain LCC variations.

Contrary to SWA (Adler et al., 2017; Schuster et al., 2013) we found no evidence of the low-level cloud formation being associated with a nocturnal low-level jet and related enhanced advection of moist maritime air. In WEA the sea–land gradient is almost orthogonal to the hemispheric wind flow. This pattern results in complex interplays between zonal and meridional atmospheric dynamics which account for changes in lower-tropospheric stability and inland cool-air advection, at the origin of variations in the extension and persistence

of LCC. The case study examined here suggests some control of the cloud cover by large-scale synoptic features, but contrary to Namibia where mid-latitude 500 hPa geopotential height variations play a major role in day-to-day variations of the coastal low-level clouds (Andersen et al., 2020), mid-tropospheric dynamics have a prominent part, by controlling the zonal flow above the PBL. Within the PBL, cold air advection is another key factor, in agreement with the statistical analysis carried out by Adebisi and Zuidema (2018) for the South Atlantic Ocean, in which a strong sensitivity of the daily cloud fraction variability to 1000-hPa horizontal temperature advection was noted north of 20° S.

On the whole, this study indicates that the Meso-NH mesoscale model has good capabilities to simulate low-level cloud occurrence during the WEA dry season, therefore enabling a better understanding of the complex and subtle variations in the lower and mid-troposphere which contribute to the low-level cloud persistence or clearing at daytime. However, this analysis is limited to a single model run for a short time period, and only a small amount of observational SYNOP data are available for verification. Other simulations with different model configurations and/or longer time periods would be helpful to strengthen conclusions about the mechanisms involved in the low-level cloud formation in this region and how well this is represented in models. Moreover, further analyses of the drivers of the WEA LCC need to be done, including diagnostics on air mass origin, subsidence and aerosol load, as carried out over the southeastern Atlantic Ocean by Fuchs et al. (2017) and Adebisi and Zuidema (2018). A specific issue is the role of aerosols combined with different large-scale meteorological conditions on the temporal variations of LCC radiative effects. Stratiform clouds are sensitive to aerosol concentration and chemical composition modifying cloud droplet distribution and radiative properties (Flossmann & Wobrock, 2019; Wood, 2012). These interactions between aerosols and clouds remain one of the largest uncertainties in climate models (IPCC 2021; Li et al., 2022). During the dry season, large amounts of biomass-burning aerosols are transported from southeastern Africa to WEA during the dry season (Solmon et al., 2021). Results from large-eddy-scale simulations suggest that both aerosol concentration and chemical composition can effectively influence the life cycle of low level stratocumulus (Delbeke et al., 2023).

ACKNOWLEDGEMENTS


This study is part of the project “Dynamics, Variability and Bioclimatic Effects of Low Clouds in Western Central Africa” (DYVALOCCA, <https://dyvalocca.osug.fr/>) funded in France by the Agence Nationale de la Recherche (contract ANR-19-CE01-0021) and in Germany by the

Deutsche Forschungsgemeinschaft (contract DFG FI 786/5-1) from January 2020 to July 2024.

DATA AVAILABILITY STATEMENT

All the data used in this work are publicly available. Meso-NH outputs are available on demand. ERA5 reanalyses are available from <https://cds.climate.copernicus.eu>. The datasets used to create the concatenated SYNOP dataset are from different sources: EECRA is available at <https://rda.ucar.edu/datasets/ds292.2/#access>. ISD is from <https://www.ncei.noaa.gov/products/land-based-station/integrated-surface-database>. SAFNWC is available upon request from the AERIS/ICARE data center (<http://icare.univ-lille1.fr/>). The raw data from the Meteosat Second Generation used to construct NMS and SAFNWC data are available here: <https://data.eumetsat.int/product/EO:EUM:DAT:MSG:HRSEVIRI#>. The concatenated SYNOP observations dataset is freely available (DOI: <https://doi.org/10.5445/IR/1000150635>). The low-cloud occurrence frequency and low-cloud fraction from SAFNWC, NMS/DMS produced in this study are available upon request.

ORCID

Alexandre Berger  <https://orcid.org/0009-0005-1100-7157>

REFERENCES

- Adebiyi, A.A. & Zuidema, P. (2016) The role of the southern African easterly jet in modifying the southeast Atlantic aerosol and cloud environments. *Quarterly Journal of the Royal Meteorological Society*, 142(697), 1574–1589.
- Adebiyi, A.A. & Zuidema, P. (2018) Low cloud cover sensitivity to biomass-burning aerosols and meteorology over the southeast Atlantic. *Journal of Climate*, 31(11), 4329–4346.
- Adler, B., Kalthoff, N. & Gantner, L. (2017) Nocturnal low-level clouds over southern West Africa analysed using high-resolution simulations. *Atmospheric Chemistry and Physics*, 17(2), 899–910.
- Aellig, R., Moron, V., Camberlin, P., Champagne, O., Philippon, N., Fink, A.H. et al. (2022) Cloud observing data of 85 stations in western Central Africa.
- Andersen, H., Cermak, J., Fuchs, J., Knippertz, P., Gaetani, M., Quinting, J. et al. (2020) Synoptic-scale controls of fog and low-cloud variability in the Namib Desert. *Atmospheric Chemistry and Physics*, 20(6), 3415–3438.
- Barker, H.W. (2008) Overlap of fractional cloud for radiation calculations in GCMs: a global analysis using CloudSat and CALIPSO data. *Journal of Geophysical Research: Atmospheres*, 113, D00A01. Available from: <https://doi.org/10.1029/2007JD009677>
- Berger, A., Barbet, C., Leriche, M., Deguillaume, L., Mari, C., Chaumerliac, N. et al. (2016) Evaluation of Meso-NH and WRF/CHEM simulated gas and aerosol chemistry over Europe based on hourly observations. *Atmospheric Research*, 176, 43–63.
- Bonekamp, P.N.J., Collier, E. & Immerzeel, W.W. (2018) The impact of spatial resolution, land use, and spinup time on resolving spatial precipitation patterns in the Himalayas. *Journal of Hydrometeorology*, 19(10), 1565–1581.
- Brient, F., Couvreur, F., Villefranche, N., Rio, C. & Honnert, R. (2019) Object-oriented identification of coherent structures in large eddy simulations: importance of downdrafts in stratocumulus. *Geophysical Research Letters*, 46(5), 2854–2864.
- Camberlin, P., Togbedji, C.F., Pergaud, J., Berger, A., Aellig, R., Fink, A.H. et al. (2023) The representation of dry-season low-level clouds over Western equatorial Africa in reanalyses and historical CMIP6 simulations. *Climate Dynamics*, 61(5), 2815–2837.
- Chaboureaud, J.P., Flamant, C., Dauhut, T., Kocha, C., Lafore, J.P., Lavaysse, C. et al. (2016) Fennec dust forecast intercomparison over the Sahara in June 2011. *Atmospheric Chemistry and Physics*, 16(11), 6977–6995. Available from: <https://doi.org/10.5194/acp-16-6977-2016>
- Champagne, O., Aellig, R., Fink, A.H., Philippon, N., Camberlin, P., Moron, V. et al. (2023) Climatology of low-level clouds over Western equatorial Africa based on ground observations and satellites. *Journal of Climate*, 36(13), 4289–4306. Available from: <https://doi.org/10.1175/JCLI-D-22-0364.1>
- Cuxart, J., Bougeault, P. & Redelsperger, J.L. (2000) A turbulence scheme allowing for mesoscale and large-eddy simulations. *Quarterly Journal of the Royal Meteorological Society*, 126(562), 1–30.
- Delbeke, L., Wang, C., Tulet, P., Denjean, C., Zouzoua, M., Maury, N. et al. (2023) The impact of aerosols on the Stratiform clouds over southern West Africa: a large-Eddy simulation study. *Atmospheric Chemistry and Physics Discussions*, 23(20), 13329–13354.
- Derrien, M. & Le Gléau, H. (2005) MSG/SEVIRI cloud mask and type from SAFNWC. *International Journal of Remote Sensing*, 26(21), 4707–4732.
- Dezfuli, A. (2017) Climate of western and central equatorial Africa. In: *Oxford research encyclopedia of climate science*. Available from: <https://oxfordre.com/climatescience/view/10.1093/acrefore/9780190228620.001.0001/acrefore-9780190228620-e-511>
- Dommo, A., Philippon, N., Vondou, D.A., Sèze, G. & Eastman, R. (2018) The June–September low cloud cover in western central Africa: mean spatial distribution and diurnal evolution, and associated atmospheric dynamics. *Journal of Climate*, 31(23), 9585–9603.
- Dommo, A., Vondou, D.A., Philippon, N., Eastman, R., Moron, V. & Aloysius, N. (2022) The ERA5's diurnal cycle of low-level clouds over Western Central Africa during June–September: dynamic and thermodynamic processes. *Atmospheric Research*, 280, 106426.
- Flossmann, A.I. & Wobrock, W. (2019) Cloud processing of aerosol particles in marine stratocumulus clouds. *Atmosphere*, 10(9), 520.
- Fotso-Kamga, G., Fotso-Nguemo, T.C., Diallo, I., Yepdo, Z.D., Pokam, W.M., Vondou, D.A. et al. (2020) An evaluation of COSMO-CLM regional climate model in simulating precipitation over Central Africa. *International Journal of Climatology*, 40(5), 2891–2912.
- Fotso-Nguemo, T.C., Vondou, D.A., Tchawoua, C. & Haensler, A. (2017) Assessment of simulated rainfall and temperature from the regional climate model REMO and future changes over Central Africa. *Climate Dynamics*, 48, 3685–3705.
- Fouquart, Y. & Bonnel, B. (1980) Computations of solar heating of the Earth's atmosphere: a new parameterization. *Beitrag zur Physik der Atmosphäre*, 53, 35–62.

- Fuchs, J., Cermak, J. & Andersen, H. (2018) Building a cloud in the southeast Atlantic: understanding low-cloud controls based on satellite observations with machine learning. *Atmospheric Chemistry and Physics*, 18(22), 16537–16552.
- Fuchs, J., Cermak, J., Andersen, H., Hollmann, R. & Schwarz, K. (2017) On the influence of air mass origin on low-cloud properties in the Southeast Atlantic. *Journal of Geophysical Research: Atmospheres*, 122(20), 11–76.
- Geleyn, J.F. & Hollingsworth, A. (1979) An economical analytical method for the computation of the interaction between scattering and line absorption of radiation. *Beitraege zur Physik der Atmosphaere*, 52, 1–16.
- Haensler, A., Saeed, F. & Jacob, D. (2013) Assessing the robustness of projected precipitation changes over central Africa on the basis of a multitude of global and regional climate projections. *Climatic Change*, 121, 349–363.
- Hannak, L., Knippertz, P., Fink, A.H., Kniffka, A. & Pante, G. (2017) Why do global climate models struggle to represent low-level clouds in the west African summer monsoon? *Journal of Climate*, 30(5), 1665–1687.
- Hersbach, H., Bell, B., Berrisford, P., Hirahara, S., Horányi, A., Muñoz-Sabater, J. et al. (2020) The ERA5 global reanalysis. *Quarterly Journal of the Royal Meteorological Society*, 146(730), 1999–2049. Available from: <https://doi.org/10.1002/qj.3803>
- Hogan, R.J. & Illingworth, A.J. (2000) Deriving cloud overlap statistics from radar. *Quarterly Journal of the Royal Meteorological Society*, 126(569), 2903–2909.
- Hu, Z.Z., Huang, B. & Pegion, K. (2008) Low cloud errors over the southeastern Atlantic in the NCEP CFS and their association with lower-tropospheric stability and air-sea interaction. *Journal of Geophysical Research: Atmospheres*, 113, D12114. Available from: <https://doi.org/10.1029/2007JD009514>
- Kenfack, K., Tamoffo, A.T., Djotang Tchotchou, L.A. & Vondou, D.A. (2023) Assessment of uncertainties in reanalysis datasets in reproducing thermodynamic mechanisms in the moisture budget's provision in The Congo Basin. *Theoretical and Applied Climatology*, 154(1), 613–626.
- Klein, S.A., Hall, A., Norris, J.R. & Pincus, R. (2017) Low-cloud feedbacks from cloud-controlling factors: A review. *Surveys in Geophysics*, 38, 1307–1329.
- Kniffka, A., Knippertz, P. & Fink, A.H. (2019) The role of low-level clouds in the west African monsoon system. *Atmospheric Chemistry and Physics*, 19(3), 1623–1647.
- Komkoua Mbienda, A.J., Guenang, G.M., Kaissassou, S., Tchakoutio Sandjon, A., Tanessong, R.S., Matho Lontio, S.L. et al. (2022) Boundary layer schemes in the regional climate model RegCM4.6 over Central Africa. *Climate Dynamics*, 58(3–4), 691–709.
- Kuete, G., Mba, W.P., James, R., Dyer, E., Annor, T. & Washington, R. (2023) How do coupled models represent the African easterly jets and their associated dynamics over Central Africa during the September–November rainy season? *Climate Dynamics*, 60(9), 2907–2929.
- Lac, C., Chaboureaud, J.P., Masson, V., Pinty, J.P., Tulet, P., Escobar, J. et al. (2018) Overview of the Meso-NH model version 5.4 and its applications. *Geoscientific Model Development*, 11(5), 1929–1969.
- Lensky, I.M. & Rosenfeld, D. (2008) Clouds-aerosols-precipitation satellite analysis tool (CAPSAT). *Atmospheric Chemistry and Physics*, 8(22), 6739–6753.
- Li, J., Carlson, B.E., Yung, Y.L., Lv, D., Hansen, J., Penner, J.E. et al. (2022) Scattering and absorbing aerosols in the climate system. *Nature Reviews Earth & Environment*, 3(6), 363–379. Available from: <https://doi.org/10.1038/s43017-022-00296-7>
- Van der Linden, R., Fink, A.H. & Redl, R. (2015) Satellite-based climatology of low-level continental clouds in southern West Africa during the summer monsoon season. *Journal of Geophysical Research: Atmospheres*, 120(3), 1186–1201.
- Lunet, T., Lac, C., Auguste, F., Visentin, F., Masson, V. & Escobar, J. (2017) Combination of WENO and explicit Runge–Kutta methods for wind transport in the Meso-NH model. *Monthly Weather Review*, 145(9), 3817–3838.
- Masson, V., Le Moigne, P., Martin, E., Faroux, S., Alias, A., Alkama, R. et al. (2013) The SURFEXv7. 2 land and ocean surface platform for coupled or offline simulation of earth surface variables and fluxes. *Geoscientific Model Development*, 6(4), 929–960.
- Mlawer, E.J., Taubman, S.J., Brown, P.D., Iacono, M.J. & Clough, S.A. (1997) Radiative transfer for inhomogeneous atmospheres: RRTM, a validated correlated-k model for the longwave. *Journal of Geophysical Research: Atmospheres*, 102(D14), 16663–16682.
- Morcrette, J.J. (1989) Comparison of satellite-derived and model-generated diurnal cycles of cloudiness and brightness temperatures. *Advances in Space Research*, 9(7), 175–179.
- Morcrette, J.J. (1991) Radiation and cloud radiative properties in the European Centre for Medium Range Weather Forecasts forecasting system. *Journal of Geophysical Research: Atmospheres*, 96(D5), 9121–9132.
- Morcrette, J.J. & Fouquart, Y. (1986) The overlapping of cloud layers in shortwave radiation parameterizations. *Journal of Atmospheric Sciences*, 43(4), 321–328.
- Moron, V., Camberlin, P., Aellig, R., Champagne, O., Fink, A.H., Knippertz, P. et al. (2023) Diurnal to interannual variability of low-level cloud cover over western equatorial Africa in May–October. *International Journal of Climatology*, 43, 6038–6064.
- Moron, V., Camberlin, P., Philippon, N., Fink, A.H. & Knippertz, P. (2025) Regional to large-scale mechanisms controlling intra-seasonal variability of low-level clouds in Western Equatorial Africa. *Quarterly Journal of the Royal Meteorological Society*, e4974. Available from: <https://doi.org/10.1002/qj.4974>
- Myers, T.A. & Norris, J.R. (2016) Reducing the uncertainty in subtropical cloud feedback. *Geophysical Research Letters*, 43(5), 2144–2148.
- Nam, C., Bony, S., Dufresne, J.L. & Chepfer, H. (2012) The ‘too few, too bright’ tropical low-cloud problem in CMIP5 models. *Geophysical Research Letters*, 39(21), 2012GL053421. Available from: <https://doi.org/10.1029/2012GL053421>
- Nicholson, S.E. & Grist, J.P. (2003) The seasonal evolution of the atmospheric circulation over West Africa and equatorial Africa. *Journal of Climate*, 16(7), 1013–1030.
- Ouhechou, A., Philippon, N., Morel, B., Trentmann, J., Graillet, A., Mariscal, A. et al. (2023) Inter-comparison and validation against in-situ measurements of satellite estimates of incoming solar radiation for Central Africa: from the annual means to the diurnal cycles. *Atmospheric Research*, 287, 106711.
- Painemal, D., Xu, K.M., Cheng, A., Minnis, P. & Palikonda, R. (2015) Mean structure and diurnal cycle of Southeast Atlantic boundary layer clouds: insights from satellite observations and multi-scale modeling framework simulations. *Journal of Climate*, 28(1), 324–341.

- Parker, D.J. & Diop-Kane, M. (Eds.). (2017) *Meteorology of tropical West Africa: the forecasters' handbook*. Chichester: John Wiley & Sons.
- Pergaud, J., Masson, V., Malardel, S. & Couvreur, F. (2009) A parameterization of dry thermals and shallow cumuli for mesoscale numerical weather prediction. *Boundary-Layer Meteorology*, 132, 83–106.
- Philippon, N., Cornu, G., Monteil, L., Gond, V., Moron, V., Pergaud, J. et al. (2019) The light-deficient climates of western central African evergreen forests. *Environmental Research Letters*, 14(3), 034007. Available from: <https://doi.org/10.1088/1748-9326/aaf5d8>
- Philippon, N., Ouhechou, A., Camberlin, P., Trentmann, J., Fink, A.H., Maloba, J.D. et al. (2022) Characterization of sunshine duration in western equatorial Africa: in situ measurements versus SARA-2 satellite estimates. *Journal of Applied Meteorology and Climatology*, 61(2), 185–201. Available from: <https://doi.org/10.1175/JAMC-D-21-0072.1>
- Pinty, J.P. & Jabouille, P. (1998) A mixed-phase cloud parameterization for use in mesoscale non-hydrostatic model: simulations of a squall line and of orographic precipitations. In: *Conf. On cloud physics*. Everett, WA: Amer. Meteor. Soc, pp. 217–220.
- Poan, D.E., Lafore, J.P., Roehrig, R. & Couvreur, F. (2015) Internal processes within the African easterly wave system. *Quarterly Journal of the Royal Meteorological Society*, 141(689), 1121–1136.
- Räisänen, P. (1998) Effective longwave cloud fraction and maximum-random overlap of clouds: a problem and a solution. *Monthly Weather Review*, 126(12), 3336–3340.
- Richter, I. & Tokinaga, H. (2020) An overview of the performance of CMIP6 models in the tropical Atlantic: mean state, variability, and remote impacts. *Climate Dynamics*, 55(9–10), 2579–2601.
- Schuster, R., Fink, A.H. & Knippertz, P. (2013) Formation and maintenance of nocturnal low-level stratus over the southern West African monsoon region during AMMA 2006. *Journal of the Atmospheric Sciences*, 70(8), 2337–2355.
- Seethala, C., Meirink, J.F., Horváth, Á., Bennartz, R. & Roebeling, R. (2018) Evaluating the diurnal cycle of South Atlantic stratocumulus clouds as observed by MSG SEVIRI. *Atmospheric Chemistry and Physics*, 18(17), 13283–13304.
- Seibert, P., Beyrich, F., Gryning, S.E., Joffre, S., Rasmussen, A. & Tercier, P. (2000) Review and intercomparison of operational methods for the determination of the mixing height. *Atmospheric Environment*, 34(7), 1001–1027.
- Seidel, D.J., Zhang, Y., Beljaars, A., Golaz, J.C., Jacobson, A.R. & Medeiros, B. (2012) Climatology of the planetary boundary layer over the continental United States and Europe. *Journal of Geophysical Research: Atmospheres*, 117, D17106. Available from: <https://doi.org/10.1029/2012JD018143>
- Solmon, F., Elguindi, N., Mallet, M., Flamant, C. & Formenti, P. (2021) West African monsoon precipitation impacted by the south eastern Atlantic biomass burning aerosol outflow. *Npj Climate and Atmospheric Science*, 4(1), 54.
- Taguela, T.N., Vondou, D.A., Moufouma-Okia, W., Fotso-Nguemo, T.C., Pokam, W.M., Tanessong, R.S. et al. (2020) CORDEX multi-RCM hindcast over Central Africa: evaluation within observational uncertainty. *Journal of Geophysical Research: Atmospheres*, 125(5), e2019JD031607.
- Tiedtke, M. (1993) Representation of clouds in large-scale models. *Monthly Weather Review*, 121(11), 3040–3061.
- Vondou, D.A. & Haensler, A. (2017) Evaluation of simulations with the regional climate model REMO over Central Africa and the effect of increased spatial resolution. *International Journal of Climatology*, 37, 741–760.
- Wood, R. (2012) Stratocumulus clouds. *Monthly Weather Review*, 140(8), 2373–2423.
- Xu, Z., Chang, P., Richter, I., Kim, W. & Tang, G. (2014) Diagnosing southeast tropical Atlantic SST and ocean circulation biases in the CMIP5 ensemble. *Climate Dynamics*, 43, 3123–3145.

How to cite this article: Berger, A., Camberlin, P., Pergaud, J., Bahuét-Bourret, Y., Aellig, R. & Champagne, O. (2025) The dry-season low-level cloud cover over western equatorial Africa: A case study with a mesoscale atmospheric model. *Quarterly Journal of the Royal Meteorological Society*, e4962. Available from: <https://doi.org/10.1002/qj.4962>